

# 3D self-consistent $N$ -body barred models of the Milky Way

## II. Gas dynamics

R. Fux

Geneva Observatory, Ch. des Maillettes 51, CH-1290 Sauverny, Switzerland

Received 26 November 1998 / Accepted 9 February 1999

**Abstract.** The gas dynamics in the Galactic disc is modeled by releasing an initially axisymmetric SPH component in a completely self-consistent and symmetry-free 3D  $N$ -body simulation of the Milky Way in which the stellar components display a COBE-like bar. The density centre of the stellar bar wanders around the centre of mass and the resulting gas flow is *asymmetric* and *non-stationary*, reproducing the HI and CO  $\ell - V$  diagrams only at specific times and thus suggesting a transient nature of the observed inner gas kinematics.

The best matching models allow a new and coherent interpretation of the main features standing out of the  $\ell - V$  data within the bar region. In particular, the  $\ell - V$  traces of the prominent offset dustlanes leading the bar major axis in early-type barred spirals can be unambiguously identified, and the 3-kpc arm and its non-symmetric galactocentric opposite counterarm are the inner prolongations of disc spiral arms passing round the bar and joining the dustlanes at very different galactocentric distances. Bania's clump 1 and 2, and another velocity-elongated feature near  $\ell = 5.5^\circ$ , are interpreted as gas lumps crossing the dustlane shocks. The terminal velocity peaks near  $\ell = \pm 2.5^\circ$  are produced by gas along the dustlanes and not by the trace of the cusped  $x_1$  orbit, which passes farther away from the Galactic centre. According to these models and to related geometrical constraints, the Galactic bar must have an inclination angle of  $25^\circ \pm 4^\circ$ , a corotation radius of 4.0 – 4.5 kpc and a face-on axis ratio  $b/a \approx 0.6$ .

**Key words:** Galaxy: structure – Galaxy/ISM: kinematics and dynamics – Galaxy: centre – Hydrodynamics – Methods: numerical

### 1. Introduction

The gas kinematics near the Galactic plane, mainly observed in HI (Burton 1985; Kerr et al. 1986; Stark et al. 1992 and Hartmann & Burton 1997),  $^{12}\text{CO}$  (Dame et al. 1987; Oka et al. 1998b),  $^{13}\text{CO}$  and CS (Bally et al. 1987), is probably among the best tracer of the dynamical mass in the Galaxy. Under the assumption of circular motion in an axisymmetric potential, the

tangent point method allows in principle to derive the rotation curve inside the solar circle and to recover the spatial location of the spiral arms (see the compilation of Vallée 1995).

However, this approach is limited for at least two reasons related to the data themselves. First, it is long known (Rougoor & Oort 1960) that the longitude-velocity ( $\ell - V$ ) distribution of the Galactic gas reveals substantial diffuse and feature-like emission in the regions ( $\ell > 0, V < 0$ ) and ( $\ell < 0, V > 0$ ) close to the Galactic centre which are forbidden to pure circular motion, the most popular example being the 3-kpc arm. Second, bumps of about  $7 \text{ km s}^{-1}$  on the terminal velocity curves near the tangent points of the spiral arms reflect the gravitational perturbation of these arms on the gas flow and can propagate into distance errors of  $\sim 1$  kpc along the line of sight if modeled by circular motion (Burton 1992; Combes 1991).

Traditional interpretations of the “forbidden” velocities near the centre involve explosion induced expansion (van der Kruit 1971; van der Kruit et al. 1972; Cohen 1975; Oort 1977) or gas moving on elliptical orbits in either a spiral (Shane 1972; Simonson & Mader 1973) or a barred potential (Peters 1975; Cohen & Few 1976; Liszt & Burton 1980; Gerhard & Vietri 1986). In the last decade, the latter interpretation received strong support by direct evidence of a large scale stellar bar in the Milky Way from near-IR surface photometry (Blitz & Spergel 1991; Dwek et al. 1995; Binney et al. 1997), discrete source counts (Nakada et al. 1991 and Izumiura et al. 1994 for SiO masers, Weinberg 1992 and Nikolaev & Weinberg 1997 for AGB stars; Whitelock & Catchpole 1992 for Miras variables; Blitz 1993 for globular clusters; Sevenster 1996 for OH/IR stars; Stanek et al. 1997 for red clump stars) and large microlensing optical depths towards the bulge (Paczynski et al. 1994; Evans 1994; Zhao et al. 1996; Zhao & Mao 1996; Gyuk 1999; see Gerhard 1996 and Kuijken 1996 for reviews).

Many hydrodynamical simulations (Roberts et al. 1979; van Albada 1985; Mulder & Liem 1986; Athanassoula 1992; Englmaier & Gerhard 1997) have shown that the gas flow in a rapidly rotating barred potential is driven by strong shocks leading the bar major axis and followed downstream by enhanced gas densities. In external early-type (i.e. Sbc and earlier) barred spirals, these shocks are detected as offset dustlanes with very large velocity changes in the associated gas velocity field (e.g. Reynaud & Downes 1998; Laine et al. 1999).

Send offprint requests to: R. Fux

Correspondence to: Roger.Fux@obs.unige.ch

Binney et al. (1991) have interpreted the gas kinematics near the Galactic centre approximating the gas streamlines by a sequence of closed  $x_1$  and  $x_2$  orbits (Contopoulos & Mertzanides 1977), but such a model does not properly care about the shocks. The hydro simulations designed for the Milky Way (Mulder & Liem 1986; Wada et al. 1994; Englmaier & Gerhard 1999; Weiner & Sellwood 1999) always assume rigid barred potentials and bisymmetry with respect to the Galactic centre, but some details in the HI and CO observations clearly betray important asymmetries: (i) about 3/4 of the molecular gas in the nuclear ring/disc lies at positive longitude, (ii) the 3-kpc arm and its far-side counterarm have very different absolute velocities at  $\ell = 0$ , and (iii) the positive and negative velocity peaks of bright emission, at  $(\ell, V/\text{km s}^{-1}) \approx (3^\circ, 270)$  and  $(-2^\circ, -220)$  respectively, differ by roughly  $50 \text{ km s}^{-1}$  in absolute velocity, and the emission of the nuclear ring/disc is also shifted towards receding velocities. Moreover, as an SBbc galaxy (Sackett 1997), the Milky Way is also expected to present prominent dustlanes, but their gaseous traces have never been convincingly isolated in the HI and CO data.

This paper follows a first paper (Fux 1997, hereafter paper I) where several  $N$ -body barred models of the Galaxy have been built from bar unstable axisymmetric initial conditions, constraining the position of the observer relative to the bar with the COBE K-band data corrected for extinction by dust. The best matching models suggested an angle of  $28^\circ \pm 7^\circ$  for the bar inclination and a corotation radius of  $4.3 \pm 0.5 \text{ kpc}$ . Here we take advantage of these simulations to seek the most convenient initial conditions for much larger simulations, including a gas component treated by the smooth particle hydrodynamics (SPH) technique and with no imposed symmetries. The resulting self-consistent gas flows are used to interpret the observed gas kinematics near the Galactic plane, and more especially within the bar region. Contrary to Weiner & Sellwood (1999), our approach is based on the observed bright  $\ell - V$  features, and not on the mostly low density gas close to the terminal velocities, for which Eulerian codes are more appropriate.

The structure of the paper is organised as follows: in Sect. 2 we describe the main features appearing in the HI and CO  $\ell - V$  diagrams within the bar region. In Sect. 3 we expose the numerical  $N$ -body and SPH code used to perform our simulations. In Sect. 4 and 5, we present the initial conditions and the time evolution of these simulations. In Sect. 6 we select some optimum models from the simulations and interpret the observed gas kinematical features. In Sect. 7 we set some new constraints on the bar parameters based on this interpretation. Finally, Sect. 8 summarises our results. Throughout the paper, we will adopt a solar galactocentric distance  $R_\odot = 8 \text{ kpc}$ .

## 2. Main observed features

In the region  $|\ell| \lesssim 30^\circ$  several features stand out from the observed longitude-velocity distribution of both atomic and molecular gas (see Figs. 1 and 2). The nomenclature of these features principally refers to Rougoor (1964) and we omit here the historical but confusing “expanding” qualification, since lo-

cal radial motions do not necessarily imply a net flux when averaged over azimuth. Other more exhaustive inventories of observed  $\ell - V$  features can be found in van der Kruit (1970) and Cohen (1975) for the HI, and in Bania (1977), Bally et al. (1988) and the review of Combes (1991) for the CO.

- *The 3-kpc arm.* This arm is the largest apparent feature, covering more than  $35^\circ$  in Galactic longitude, and with a “forbidden” radial velocity of  $-53 \text{ km s}^{-1}$  at  $\ell = 0$ . It was discovered by van Woerden et al. (1957) and its name is related to the location of its tangent point near  $\ell = -22^\circ$ , corresponding to  $R = 3 \text{ kpc}$  (at this time the galactocentric distance of the Sun was assumed to be  $8.2 \text{ kpc}$ ). The same authors also noticed that this arm must lie in front of the Galactic centre because of absorbing the continuum spectrum of radio sources close to the centre (see the HI  $\ell - V$  diagram at  $b = 0$  in Fig. 2), which is consistent with its rather large latitudinal width. The 3-kpc arm cannot be represented by a uniformly rotating and expanding circular arc over its whole longitude range (Burke & Tuve 1964). It was successfully modeled by Mulder & Liem (1986) as a stationary density wave in a rotating barred potential.
- *The 135-km s<sup>-1</sup> arm.* This feature shows no absorption lines against Galactic centre radio sources and is suspected to be the far-side counterpart of the 3-kpc arm (e.g. Oort 1977). However it crosses the zero longitude axis at  $135 \text{ km s}^{-1}$  (hence his name), i.e. more than twice the absolute velocity of the 3-kpc arm, which is among the strongest evidence for an asymmetric spiral structure in the central few kpc (velocity asymmetries at  $\ell = 0$  cannot result from perspective effects). The 135-km s<sup>-1</sup> arm extends down to  $\ell \approx -5^\circ$ , where its radial velocity still reaches about  $100 \text{ km s}^{-1}$ , and lies slightly above the Galactic plane, at  $b \approx 0.5^\circ$ . It also involves less HI mass than the 3-kpc arm and is more lumpy.
- *The connecting arm.* This is a very rarely discussed feature in the recent literature, despite its substantial brightness. It was probably mentioned the first time by Rougoor & Oort (1960). The origin of its name comes from the fact that it seems to link the nuclear ring/disc to the outer disc. It becomes easily identifiable in the HI and <sup>12</sup>CO data near  $\ell = 10^\circ$  and  $V = 110 \text{ km s}^{-1}$ , where it is located far below the plane at  $b \approx -1^\circ$ , and passes through the peak of the positive terminal velocity curve. In Rougoor’s (1964) description, this feature is doubtfully combined with another distinct feature extending at roughly constant velocity out to  $\ell \approx 18^\circ$ . The connecting arm was soon recognized as a very inclined spiral arm, i.e. with a high pitch angle, although its situation in front or behind the Galactic centre remained unclear (Rougoor 1964; Cohen & Davies 1976). Kerr (1967) adopted the latter alternative and interpreted this arm as part of a central gaseous bar.
- *The nuclear ring/disc, or central molecular zone.* Concerns the offcentred dense molecular gas located within  $-1^\circ \lesssim \ell \lesssim 1.5^\circ$ , i.e. somewhat inside the positive and negative peaks of the terminal velocity curves (see for instance

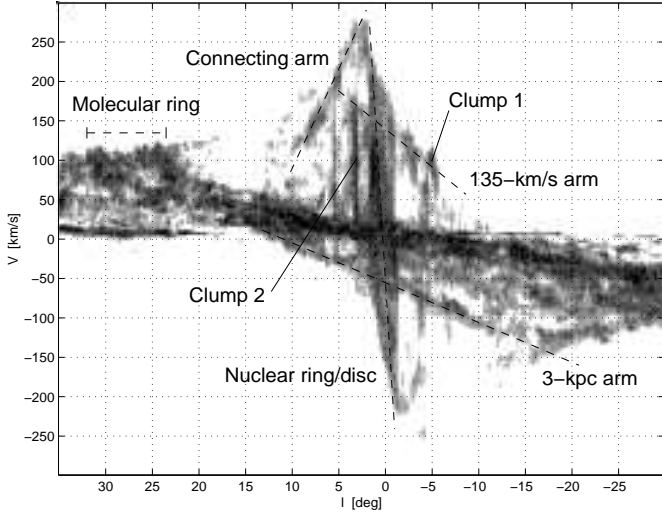
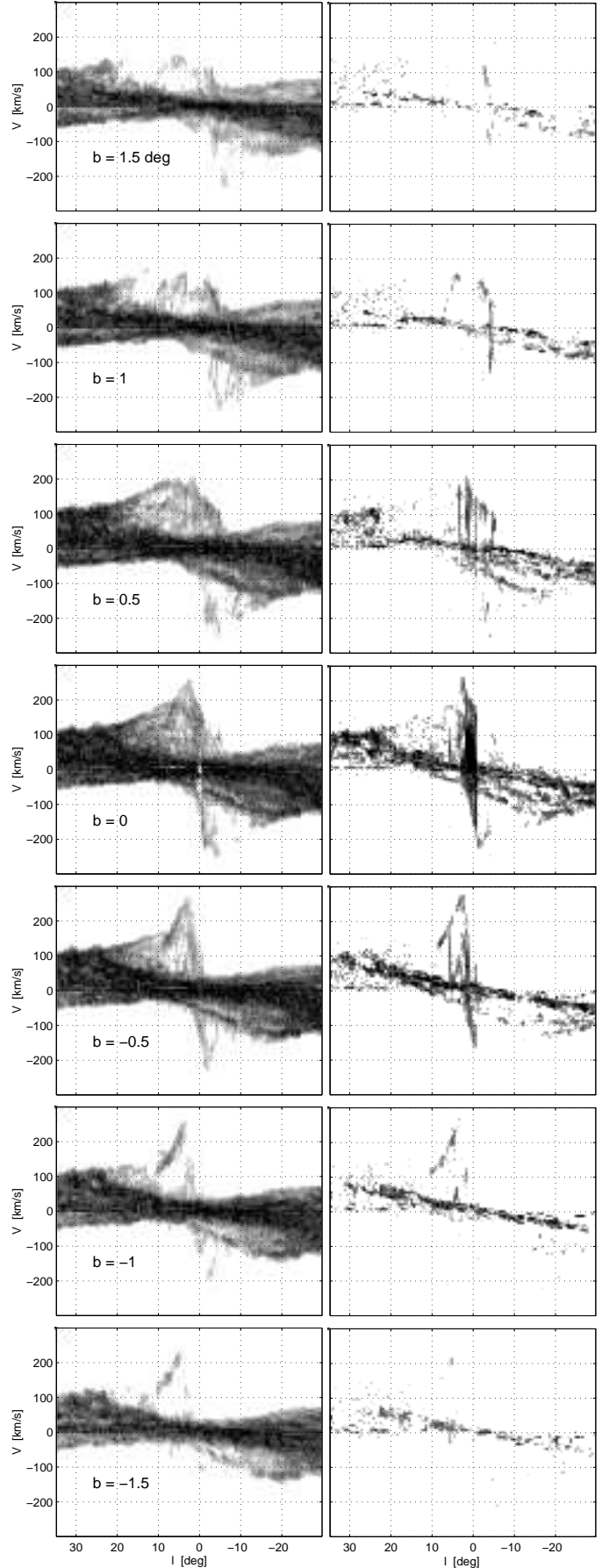


**Fig. 1.** Grey scale longitude-velocity diagram of  $^{12}\text{CO } J = 1 \rightarrow 0$  emission within  $-30^\circ \leq \ell \leq 35^\circ$  and over a  $4^\circ$  latitude strip centred on the Galactic plane (Dame et al. 1999), with the dominant features indicated by dashed lines and Bania’s (1977) molecular clumps.

**Fig. 2.** (right column) Longitude-velocity diagrams of HI 21 cm (left) and  $^{12}\text{CO } J = 1 \rightarrow 0$  (right) emission as a function of longitude in the range  $|b| \leq 1.5^\circ$ . The HI data are from Hartmann & Burton (1997), Burton & Liszt (1978) and Kerr et al. (1986), and the CO data from Dame et al. (1987).



the high resolution CO  $\ell - V$  maps in Oort 1977; Liszt & Burton 1978; Bally et al. 1988; Combes 1991; Morris & Serabyn 1996 and Oka et al. 1998b). The parallelogram bounding this structure is also called “expanding molecular ring” owing to its original interpretation (Scoville 1972; Kaifu et al. 1972), and more recently “180-pc ring” according to its size. The molecular complex enclosed by this ring forms a kind of disc rotating with a maximum velocity of order  $100 \text{ km s}^{-1}$  and is speculated to form two mini spirals (Sofue 1995). Almost the entire CS emission comes from this disc. Binney et al. (1991) have interpreted the parallelogram and the disc respectively as gas on the cusped  $x_1$  orbit and on  $x_2$  orbits in the bar potential (see Sect. 6.5). An extensive review on this pattern is given by Morris & Serabyn (1996).

- *The molecular ring.* Meant to represent a ring-like gas concentration with a radius of roughly 4 kpc, the spatial distribution of this structure is in fact poorly known and could as well involve imbricated spiral arms. Close to the positive terminal velocity curve, it forms two branches with tangent points at  $\ell \approx 25^\circ$  and  $30^\circ$ , corresponding to  $R \approx 3.4$  kpc and 4 kpc. The molecular ring probably compares to the inner (pseudo-) rings seen in external spiral galaxies (Buta 1996).

All features listed here appear both in the CO and HI data with a rigorous coincidence in position, although the central molecular zone is much weaker in HI. It is not yet clear whether

these features are transient or represent a permanent gas flow on closed orbits.

Bania (1977) has also isolated two particular “clumps” in the  $^{12}\text{CO}$  data (see Fig. 1), corresponding to massive molecular cloud complexes.

- *Clump 1* is located at the negative longitude end of the  $135\text{-km s}^{-1}$  arm, at  $\ell \approx -5^\circ$  and  $b \approx 0.4^\circ$ , and represents the most extreme case of non-circular motion in the Milky Way’s dense gas kinematics. It is located at slightly lower latitude than the nearby emission from the  $135\text{-km s}^{-1}$  arm. The clump 1 complex has been resolved into three distinct sub-complexes each of about  $2.5 \times 10^5 M_\odot$   $\text{H}_2$  mass. More details on its physical properties are presented in Bania et al. (1986).
- *Clump 2* is confined near  $\ell = 3^\circ$  and  $b = 0.2^\circ$  and spans an extraordinary large velocity range of over  $150 \text{ km s}^{-1}$ . It has been resolved into 16 emitting cores of  $\sim 5 \times 10^5 M_\odot$  by Stark & Bania (1986), who also interpret this clump as a dustlane or an inner spiral arm in a barred potential formed by molecular clouds distributed along the line of sight.

The CO is usually considered as a tracer of  $\text{H}_2$ , although it is now well established that the density ratio between these two molecules is not homogeneous in galaxies. Beside the  $2.6 \text{ mm } ^{12}\text{CO } J = 1 \rightarrow 0$  emission line, other more transparent molecular tracer like  $^{12}\text{CO } J = 2 \rightarrow 1$  (Oka et al. 1998a),  $^{13}\text{CO}$  and CS (Bally et al. 1987), as well as HCN (Jackson et al. 1996; Lee 1996), have also been used to map dense gas like in the Galactic centre region.

The interpretation of features in the  $\ell - V$  diagrams is subject to many difficulties. First, since only the radial component of the velocity is measured, the in-plane velocity field can be recovered directly only under very restrictive symmetry assumptions like axisymmetry. Second, some features may not trace real spiral arms but be artifact of velocity crowding along the line of sight (Burton 1973; Mulder & Liem 1986). Third, features elongated in the velocity direction can be understood either by real structures elongated along the line of sight or by spatially localised emission with a very large velocity spread, as would result for example in a supernova explosion or in violent shocks. Finally, some regions in the  $\ell - V$  space overlay the emission from several distinct sources, in particular the low velocity emission from the Galactic centre region is partly hidden by the emission from the surrounding disc spiral arms. This problem can however be addressed considering the latitudinal gas distribution or resorting to very dense gas tracers. Optically thick regions are also strongly affected by absorption.

### 3. Numerical methods

The initial models are evolved using a composite  $N$ -body and hydro code developed by the Geneva Observatory galactic dynamic group, originally provided by D. Friedli but considerably modified in the present application. At each time step, the gravitational forces on all particles (gas included) are derived by

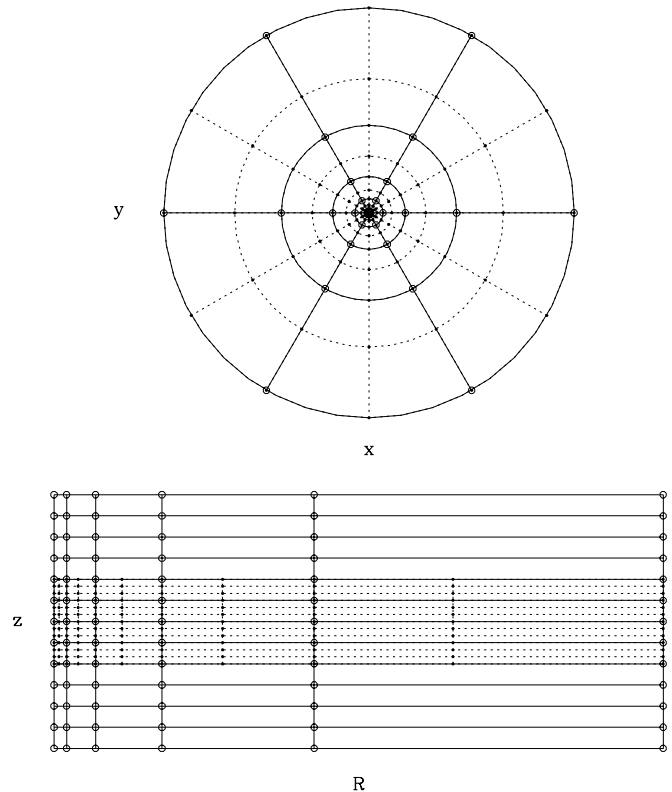


**Fig. 3.** Example of a double grid with  $N_R = 10$ ,  $N_\phi = 12$ ,  $N_z = 13$  and  $M_z = 3$ . The solid points and dotted lines are the points and meshes of grid A, and the circles and solid lines those of grid B.

the particle-double mesh method detailed in Sect. 3.1, the pressure and viscous forces on the gas particles by the Lagrangian smoothed particle hydrodynamics (SPH) technique described in Sect. 3.2, and finally the phase space coordinates of each particle are updated by integration of the equations of motion according to the algorithm presented in Sect. 3.3.

#### 3.1. Gravitation with $\text{PM}^2$

To compute the gravitational forces on the particles, we have resorted as in paper I to the particle-mesh (PM) technique with polar-cylindrical grid geometry and variable homogeneous ellipsoidal kernel for the softening of the short range forces (Pfenniger & Friedli 1993). However, instead of using a single grid with constant vertical resolution, inappropriate to model efficiently the high density contrast between a thin disc and an extended dark halo, we have introduced a double embedded grid structure. The higher resolution grid (A) has  $N_R \times N_\phi \times N_z$  cells, with a maximum radial extent  $R_{\text{max}}$  and a vertical spacing  $H_z$ , i.e.  $z_{\text{max}}^A = (N_z - 1)/2 \cdot H_z$ . The lower resolution grid (B) has half the number of cells in each dimension of the plane, skipping every second  $R$ - and  $\phi$ -grid point of the finer grid, and the same number of cells vertically but with a spacing of  $M_z \cdot H_z$ , i.e.  $z_{\text{max}}^B = M_z \cdot z_{\text{max}}^A$ . Hence grid B has the same radial extent than grid A, but is larger in the vertical dimension.

Both grids have constant vertical spacing, thus allowing to keep the advantage of the Fast Fourier Transform algorithm in this dimension. Here  $N_z$  designates the number of active cells in  $z$ , corresponding to half the value required by the doubling-up method (Hockney & Eastwood 1981). The vertical grid parameters are chosen to satisfy:

$$N_z = 1 + 2k \cdot M_z, \quad k \text{ integer } \geq 2, \quad (1)$$

ensuring that (i) there are grid points of each grid in the plane  $z = 0$ , (ii) the horizontal planes  $z = \pm z_{\text{max}}^A$  delimiting vertically grid A also contain points of grid B, and (iii) grid B has at least four cells within grid A in the  $z$  dimension. Figure 3 gives an example of double grid fulfilling all these conditions.

In this particle-double mesh (or  $\text{PM}^2$ ) method, the mass assignment to the grid cells is repeated twice (once for each grid), and the total potential involves the evaluation of three sub-potentials:  $\Phi_A$  and  $\Phi_B$  generated by the mass inside grids A and B respectively, as well as  $\Phi_C$  generated by the mass within grid B but outside grid A. The potential  $\Phi_A$  is computed on grid A, at high resolution, and the other potentials on grid B. The total potential then amounts to  $\Phi_A + \Phi_C$  in the region of grid A, which requires an interpolation of  $\Phi_C$  to grid A, and simply to  $\Phi_B$  outside this region. The increase of CPU time owing to the triple potential evaluation is amply compensated by the reduction by a factor  $\sim M_z$  of the effective number of cells relative to a single grid with the same resolution as grid A and the same size as grid B. The transition planes between the two grids are associated with numerical discontinuities in the force components, although quite small in practice (see Fig. 4). To smooth them out, the forces in the first and last cells of grid B within grid A are taken as a linear combination so that the forces at  $z = \pm z_{\text{max}}^A$  coincide with the forces of grid B and those at  $z = \pm(z_{\text{max}}^A - M_z H_z)$  with the forces of grid A.

The grid parameters adopted in our simulations are given in Table 1 and the resulting gravitational resolution achieved with the high resolution double grid is depicted in Fig. 5.

### 3.2. Gas hydrodynamics with SPH

The pressure and viscous forces acting on the gas particles are derived by three-dimensional SPH. We will not repeat here the principle of this very popular Lagrangian method for solving Euler's equation of motion (see Benz 1990; Monaghan 1992 and Steinmetz 1996 for reviews), but just give the necessary specifications about this part of our code.

The relevant form of the Euler equation writes:

$$\frac{d\mathbf{v}}{dt} \equiv \frac{\partial \mathbf{v}}{\partial t} + (\mathbf{v} \cdot \nabla) \mathbf{v} = -\frac{\nabla P}{\rho} - \Pi - \nabla \Phi, \quad (2)$$

where  $\mathbf{v}(\mathbf{r})$  is the velocity field,  $\rho(\mathbf{r})$  the spatial mass density and  $P(\mathbf{r})$  the pressure of the gas.  $\Pi$  is the viscosity term and  $-\nabla \Phi$  the gravitational force as obtained by the  $\text{PM}^2$  method.

The internal properties of a classical fluid are fully described by three macroscopic independent variables of state,

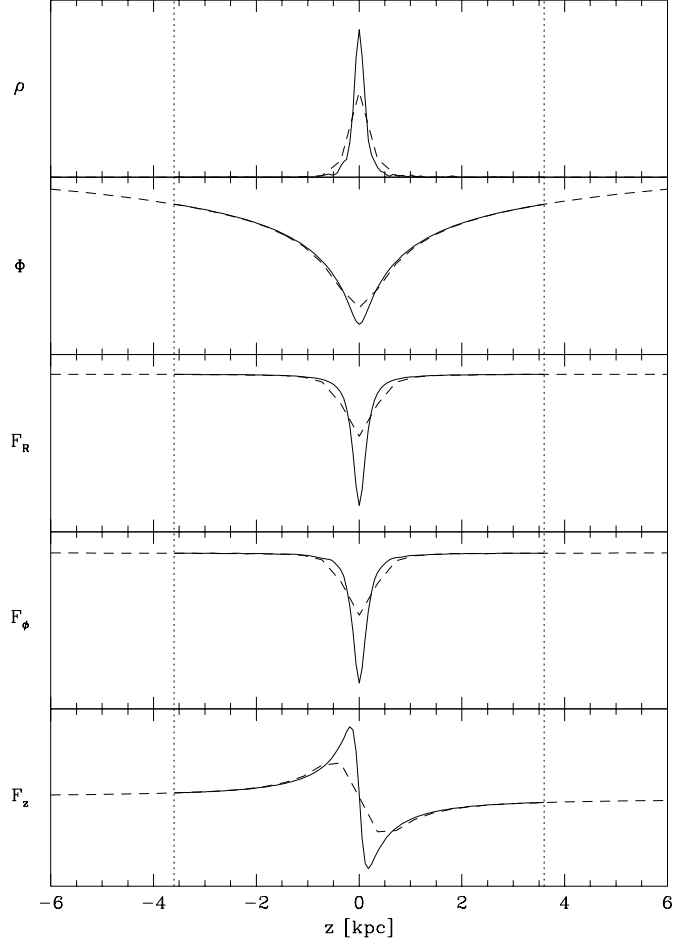


**Fig. 4.** Typical  $z$ -behaviour of model dynamical properties calculated with the high resolution double grid, i.e.  $N_R = 62$ ,  $N_\phi = 64$ ,  $N_z = 121$ ,  $M_z = 6$ ,  $R_{\text{max}} = 50$  kpc and  $H_z = 60$  pc (the mass distribution and the grid refer to model 110t2000). From top to bottom and in linear scales: mass density ( $\rho$ ), potential ( $\Phi$ ) and the three force components ( $F_R$ ,  $F_\phi$  and  $F_z$ ). The full lines are the results from grid A (based on  $\Phi_A + \Phi_C$ ), and the dashed lines those from grid B (based on  $\Phi_B$ ). The vertical dotted lines indicate the limits  $z = \pm z_{\text{max}}^A$  of grid A. The forces considerably differ from one grid to the other near the plane  $z = 0$ , but almost confound in the transition zone.

like for example the density and the pressure appearing explicitly in Eq. (2), and the internal energy per unit mass  $u(\mathbf{r})$ . The density is evaluated directly at each particle position  $\mathbf{r}_i$  via:

$$\rho_i \equiv \rho(\mathbf{r}_i) = \sum_{j=1}^{N_g} m_j W(\mathbf{r}_i - \mathbf{r}_j, h), \quad (3)$$

where  $N_g$  is the number of gas particles,  $m_j$  the individual mass of the particles,  $W(\mathbf{r}, h)$  the kernel function and  $h$  the smoothing length. In SPH, this equation is equivalent to the continuity equation expressing the conservation of total mass.

A first relation between the variables of state is given by the equation of state assuming a perfect gas, i.e.  $P = (\gamma - 1)\rho \cdot u$ ,

where  $\gamma$  is the adiabatic index of the gas, which from statistical mechanics is given by  $\gamma = 1 + 2/f$ , with  $f$  being the number of freedom degrees of the gas constituents ( $f = 3$  for atomic hydrogen and  $f = 5$  for molecular hydrogen). A second relation comes from the energy conservation equation, which in its general form involves cooling and heating functions. Since these functions are poorly constrained by theory, we have simply resorted to the isothermal assumption, i.e. the internal energy of the gas is at any time and everywhere the same. This assumption, partly justified by the homogeneous velocity dispersion of the warm gas component in external galaxies (e.g. van der Kruit & Shostak 1984), means that cooling and heating exactly cancel each other and that the energy released by the shocks is instantaneously radiated away. Hence, introducing the (constant) sound speed  $c_s = [\gamma(\gamma - 1) \cdot u]^2$  to substitute the internal energy, the equation of state for particle  $i$  reduces to:

$$P_i = \frac{c_s^2}{\gamma} \cdot \rho_i, \quad (4)$$

which is degenerated in sound speed and adiabatic index, depending only on the ratio  $c_s^2/\gamma$ . With this last equation, Benz's (1990) SPH version of the pressure term in Euler's equation simply becomes:

$$\left(\frac{\nabla P}{\rho}\right)_i \approx -\frac{c_s^2}{\gamma} \cdot \sum_{j=1}^{N_g} m_j \left(\frac{1}{\rho_i} + \frac{1}{\rho_j}\right) \nabla_i W(\mathbf{r}_i - \mathbf{r}_j, h). \quad (5)$$

The empirical artificial viscosity is calculated exactly as in Benz (1990). It consists of a superposition of the ‘‘bulk’’ and the von Neumann-Richtmyer viscosities, with the standard parameters set to  $\alpha = 1.0$  and  $\beta = 2.5$ , and takes into account Balsara's (1995) correction to avoid energy dissipation in pure shearing flows.

We have used the spherical spline kernel because of its finite spatial extension:

$$W(\mathbf{r}, h) = \frac{1}{\pi h^3} \begin{cases} 1 - \frac{3}{2}w^2 + \frac{3}{4}w^3 & \text{if } 0 \leq w \leq 1, \\ \frac{1}{4}(2-w)^2 & \text{if } 1 \leq w \leq 2, \\ 0 & \text{if } w \geq 2, \end{cases} \quad (6)$$

where  $w \equiv |\mathbf{r}|/h$ . To increase the hydro resolution in high density regions like shocks, the particles are assigned individual smoothing lengths  $h_i$  such that their number of neighbouring particles  $N_i$  always remains close to a fixed number  $N_o$ . Two particles  $i$  and  $j$  are defined as mutual neighbours if  $i \neq j$  and  $|\mathbf{r}_i - \mathbf{r}_j| < 2h_{ij}$ , where  $h_{ij} = (h_i + h_j)/2$  is the symmetrised smoothing length which should enter the kernel evaluations in Eqs. (3) and (5) to ensure momentum conservation.

At each time step, the smoothing lengths are updated considering the general three-dimensional scaling law:

$$\frac{h_i}{h_o} = \left(\frac{N_i + 1}{N_o + 1} \frac{\rho_o}{\rho_i}\right)^{1/3}, \quad (7)$$

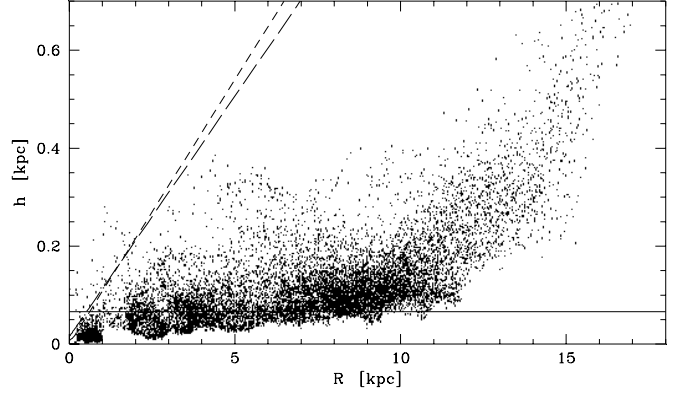


**Fig. 5.** Various spatial resolutions of the high resolution simulations presented in this paper, as a function of galactocentric radius. The solid, short dashed and long dashed lines respectively represent the vertical, azimuthal and radial semi-axes of the gravitational homogeneous ellipsoidal kernel associated with grid A, and the points are the smoothing lengths of a random selection of 10% SPH particles in model 110t2000. The gas smoothing length is close to the vertical gravitational resolution.

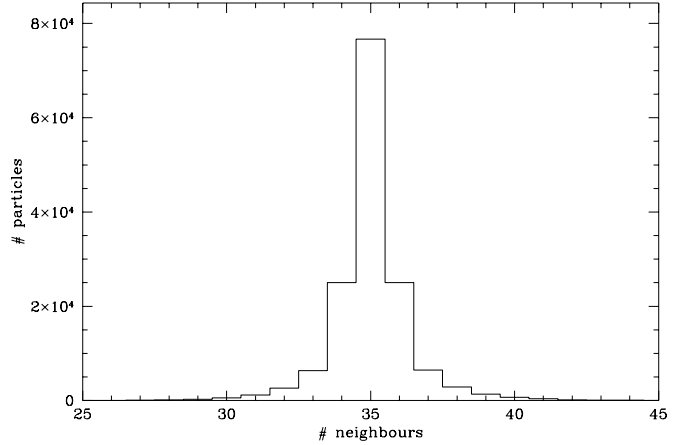


**Fig. 6.** Typical distribution of the number of neighbouring SPH particles, obtained by adjusting at each time step the smoothing lengths according to Eqs. (8) and (9). The data refer to model 110t2000.

where  $h_o$  and  $\rho_o$  are constants, and +1 is added to account for particle  $i$ . Following Benz (1990), differentiating this formula and substituting the continuity equation yields:

$$\dot{h}_i \equiv \frac{dh_i}{dt} = \frac{1}{3} h_i \left( \frac{1}{N_i + 1} \frac{dN_i}{dt} + [\nabla \cdot \mathbf{v}]_i \right). \quad (8)$$

Benz did only consider the variation of  $h_i$  ensuring the constancy of the neighbour numbers, and hence did not include the term in  $N_i$ . However, in practice, numerical fluctuations of the  $N_i$ 's can carry these number outside a reasonable range

around  $N_o$ . To overcome this problem, we simply damp the systematic departure of the  $N_i$ 's from  $N_o$  setting:

$$\frac{dN_i}{dt} = \frac{N_i - N_o}{\eta \Delta t} \quad (9)$$

in Eq. (8) and integrate the resulting equation along with the equations of motion (see Sect. 3.3). The parameter  $\eta$  controls the damping rate per time step ( $\Delta t$ ) and should be significantly greater than 1 to avoid abrupt discontinuities in the non-gravitational forces. In all simulations we have adopted  $N_o = 35$  and  $\eta = 5$ . Figure 5 shows the typical SPH resolution achieved in evolved models and Fig. 6 an example of the neighbour number distribution. The standard deviation of this distribution usually amounts to only about 1.5 neighbours. The velocity divergence in Eq. (8), which is also needed for the viscous forces, is estimated as in Benz (1990).

The initial smoothing lengths of the gas particles, confined near the plane  $z = 0$ , are derived from the two-dimensional scaling relation:

$$h_i(t = t_o) = \sqrt{\frac{N_o m_i}{4\pi \Sigma_g(R_i)}}, \quad (10)$$

where  $\Sigma_g(R)$  is the surface mass density profile of the gas component and  $t_o$  its switch-on time (see Sect. 5). This method unfortunately leads to a large spread in the initial neighbour numbers. To adjust the  $h_i$ 's without evolving too much the system, the simulations with live gas are therefore started with a time step much smaller than in the subsequent stabilised regime, i.e.  $\Delta t = 0.001$  Myr for the large simulations (l-series) and  $\Delta t = 0.01$  Myr for the smaller ones (s-series).

### 3.3. Integrator

To integrate the equations of motion, we have applied a semi-adaptative second order accurate algorithm where the (Cartesian) phase space coordinates, contrary to the standard leap-frog scheme, are evaluated at synchronous times. At each time step the positions  $\mathbf{r}_i$  and velocities  $\mathbf{v}_i$  of the particles are modified according to (e.g. Hut et al. 1995):

$$\mathbf{r}_i^{n+1} = \mathbf{r}_i^n + \mathbf{v}_i^n \Delta t^n + \frac{1}{2} \mathbf{a}_i^n (\Delta t^n)^2, \quad (11)$$

$$\mathbf{v}_i^{n+1} = \mathbf{v}_i^n + \frac{1}{2} (\mathbf{a}_i^n + \mathbf{a}_i^{n+1}) \Delta t^n, \quad (12)$$

$$h_i^{n+1} = h_i^n + \frac{1}{2} (\dot{h}_i^n + \dot{h}_i^{n+1}) \Delta t^n, \quad (13)$$

where the  $\mathbf{a}_i$ 's are the accelerations and  $\Delta t$  is the time step, and where the last equation is used to update the smoothing lengths of the SPH particles. The indices  $n$  and  $n+1$  refer to the values at time  $t^n$  and  $t^{n+1} = t^n + \Delta t^n$  respectively.

The first equation handling the positions is not exactly reversible in time. However, we have repeated simulation m00 of paper I replacing successively the leap-frog integrator by this algorithm and a second order Runge-Kutta-Fehlberg algorithm (RKF; Fehlberg 1968) as in Friedli's original code, and found

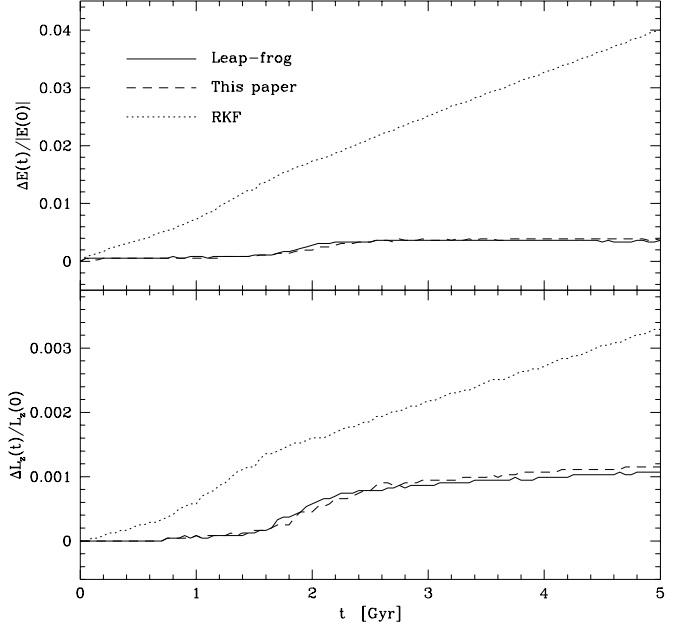


**Fig. 7.** Variation of the total energy (top) and of the total angular momentum about the rotation axis (bottom) for simulations started from the same initial conditions but evolved using three different second order integrators with the same constant time step;  $\Delta E(t) \equiv E(t) - E(0)$  and  $\Delta L_z(t) \equiv L_z(t) - L_z(0)$ . The steeper part of the curves are associated with the epoch of bar formation.

that, for the same constant time step  $\Delta t = 0.1$  Myr, the conservation of the total energy (and of the total angular momentum) is similar for the present algorithm and for the leap-frog, but much worse for the RKF ( $\Delta E/|E|$  larger by a factor  $\sim 20$ , see Fig. 7). Also, the bar begins to form much sooner with the RKF integrator, at  $t \sim 800$  Myr instead of  $\sim 1600$  Myr with the other two integrators, which is a sign of higher numerical noise amplification.

For the gaseous particles, the pressure and viscous forces contributing to  $\mathbf{a}_i^{n+1}$  both involve velocities which are not known a priori, and similarly  $\dot{h}_i^{n+1}$  depends on  $h_i^{n+1}$  (through Eq. (8)). Therefore the non-gravitational part of  $\mathbf{a}_i^{n+1}$  and  $\dot{h}_i^{n+1}$  are calculated with the first order predictors:

$$\mathbf{v}_i^p = \mathbf{v}_i^n + \mathbf{a}_i^n \Delta t^n, \quad (14)$$

$$h_i^p = h_i^n + \dot{h}_i^n \Delta t^n, \quad (15)$$

which fortunately preserve the second order accuracy of  $\mathbf{r}_i^{n+1}$ ,  $\mathbf{v}_i^{n+1}$  and  $h_i^{n+1}$ .

To temporally resolve the high density shocks in the gas component, we use an adaptative time step procedure inspired from Friedli (1992). After step  $n$ , the next time step  $\Delta t^{n+1}$  is estimated from the maximum relative contribution per unit time of the second order terms to the integrated quantities:

$$\epsilon_{\max}^{n+1} = \text{Max}_i \{ \epsilon(\mathbf{r}_i^{n+1}), \epsilon(\mathbf{v}_i^{n+1}), \epsilon(h_i^{n+1}) \}, \quad (16)$$

where

$$\epsilon(\mathbf{r}_i^{n+1}) = \frac{1}{2} \frac{|\mathbf{v}_i^{n+1} - \mathbf{v}_i^n|}{\sqrt{|\mathbf{r}_i^{n+1}|^2 + r_{\text{lim}}^2}}, \quad (17)$$

$$\epsilon(\mathbf{v}_i^{n+1}) = \frac{1}{2} \frac{|\mathbf{a}_i^{n+1} - \mathbf{a}_i^n|}{\sqrt{|\mathbf{v}_i^{n+1}|^2 + v_{\text{lim}}^2}}, \quad (18)$$

$$\epsilon(h_i^{n+1}) = \frac{1}{2} \frac{|\dot{h}_i^{n+1} - \dot{h}_i^n|}{\sqrt{(h_i^{n+1})^2 + h_{\text{lim}}^2}}, \quad (19)$$

and where  $r_{\text{lim}} = h_{\text{lim}}$  and  $v_{\text{lim}} = h_{\text{lim}}/\Delta t^n$  are destined to prevent divergences and a drastic drop of the time step. The value of  $h_{\text{lim}}$  is fixed to 0.01 pc in the large simulations and to 0.02 pc in the smaller ones, corresponding approximatively to the smallest dimension of the PM<sup>2</sup> cells. Ideally, to guarantee a relative uncertainty of the same order or smaller than a given tolerance  $E_{\text{tol}}$ , it suffice to take  $\Delta t^{n+1} = E_{\text{tol}}/\epsilon_{\text{max}}^{n+1}$ . However, a more advisable prescription is:

$$\Delta t^{n+1} = \text{Max} \{ \text{Min} [\alpha^{n+1} \cdot \Delta t^n, \Delta t_{\circ}], \Delta t_{\text{min}} \}, \quad (20)$$

with

$$\alpha^{n+1} = \text{Min} \left\{ \sqrt{\beta^{n+1}}, \alpha_{\text{max}} \right\}, \quad (21)$$

$$\beta^{n+1} = \frac{E_{\text{tol}}}{\epsilon_{\text{max}}^{n+1} \Delta t^n}, \quad (22)$$

and  $\alpha_{\text{max}} = 2$ . The square root over  $\beta^{n+1}$  softens the variations of the time step and  $\alpha_{\text{max}}$  puts an upper limit on its growth. Moreover the time step is maintained in the range  $\Delta t_{\text{min}} \leq \Delta t \leq \Delta t_{\circ}$ , with  $\Delta t_{\text{min}} = 10^{-3}$  Myr and  $\Delta t_{\circ} = 0.1$  Myr. The upper boundary is a fraction of the time needed by the stars to cross the central high resolution PM<sup>2</sup> cell in the steep nuclear potential. This time-stepping criterion is applied only to the gas, i.e. the loop on  $i$  in Eq. (16) is restricted to the gas particles, and  $\epsilon_{\text{max}}^{n+1}$  is in general controlled by the smoothing lengths.

If  $\beta < 2/3$  and  $\Delta t^n > \Delta t_{\text{min}}$ , the tolerance is considered as not respected in the last integration step. In this case, the old values of the integrated quantities are restored and integrated again with a time step  $\Delta t^n = \text{Max} \{ \sqrt{\beta^{n+1}} \cdot \Delta t^n, \Delta t_{\text{min}} \}$ . This rejection procedure unfortunately requires to store the old positions of all particles.

In the simulations with live gas, the tolerance has been set to  $E_{\text{tol}} = 10^{-1}$ , and in the simulations with fixed gas component, a constant time step  $\Delta t = \Delta t_{\circ}$  has been applied.

#### 4. Initial conditions

The radial distribution of molecular gas in the Milky Way, as traced by CO, is essentially confined inside the solar circle, with a marked hole between 1 and 3 kpc and a strong central concentration associated to the nuclear ring/disc, whereas the HI presents a rather constant surface density extending far beyond  $R_{\circ}$  and an abrupt decline towards the centre below 3 kpc. The total gas mass within  $R_{\circ}$  is estimated to  $4.2 \times 10^9 M_{\odot}$ ,

comprising  $2.3 \times 10^9 M_{\odot}$  of H<sub>2</sub> (with a large uncertainty owing to the poorly known CO to H<sub>2</sub> conversion factor) and  $0.7 \times 10^9 M_{\odot}$  of HI (Scoville 1992), plus 28% of helium and metals. For the gaseous disc, we have used the following initial mass distribution:

$$\rho_{\text{g}}(R, z) = \frac{M_{\text{g}}}{(2\pi)^{3/2} \sigma^2 p R} \exp \left[ -\frac{1}{2} \left( \frac{R^2}{\sigma^2} + \frac{z^2}{p^2 R^2} \right) \right], \quad (23)$$

with  $\sigma = 5$  kpc,  $p = 0.017$  and a total mass  $M_{\text{g}} = 5 \times 10^9 M_{\odot}$ , resulting in  $3.6 \times 10^9 M_{\odot}$  within the solar circle. Both radial and vertical profiles are Gaussian, and the disc is linearly flaring with radius, as observed in HI from a few kpc of the centre out to at least  $2R_{\circ}$  (Merrifield 1992), achieving a thickness of 136 pc at  $R = R_{\circ}$ . The fast radial decline is aimed to spare SPH particles in the outer regions and hence increase the spatial resolution near the centre at fixed number of particles. The observed gas deficit between 1 and 3 kpc needs not to be reproduced since shocks will naturally deplete this region. The gas particles initially have pure circular velocities derived from the axisymmetric part of the total potential at  $z = 0$ .

The stellar and dark mass is divided into the same three components as in paper I: a stellar nucleus-spheroid (NS), a stellar disc and a dark halo (DH), with their initial axisymmetric mass distribution described by the same analytical formulae, except for the disc. In paper I we indeed noted that the adopted double exponential discs evolve into discs with too less mass outside the bar region according to the COBE/DIRBE near-IR and bulge microlensing data, and possibly an excess of mass in the central region when compared to the HI terminal velocity constraints. Instead of increasing the disc scale length, we choose here to soften the initial central mass density taking:

$$\rho_{\text{d}}(R, z) = g(z/h_z) \frac{M_{\text{d}}}{2\pi h_R^2 h_z [\exp(-1) + \exp(-1/2)]} \cdot \begin{cases} \exp[-\frac{1}{2}(1 + \frac{R^2}{h_R^2})] & \text{if } R \leq h_R, \\ \exp[-\frac{R}{h_R}] & \text{if } R \geq h_R, \end{cases} \quad (24)$$

where  $M_{\text{d}}$  is the total disc mass,  $h_R$  the scale length,  $h_z$  the scale height and  $g(\zeta)$  the normalised vertical profile. The surface density remains exponential in the external disc, but continuously and differentiably joins an inner Gaussian distribution at  $R = h_R$ , with a central value reduced by 40% relative to the purely exponential case. To compensate for the enhanced spatial density near the plane  $z = 0$  caused by the additional gas component, we also replace the exponential vertical profile of paper I by van der Kruit's (1988) profile:

$$g(\zeta) \propto \text{sech}^{2/n} \left[ \frac{n}{2} \zeta \right], \quad (25)$$

with  $n = 7$ , between the exponential ( $n = \infty$ ) and isothermal ( $n = 1$ ) cases.

The choice of the parameters are based on the simulations performed in paper I, giving a strong weight to the  $x_1$  orbits versus HI terminal velocities test. The best models regarding this test are m06t4600 and m04t3000, whose initial axisymmetric models share the following interdependent properties:



**Table 1.** List and characteristics of the simulations presented in this paper.  $N_R$ ,  $N_\phi$ ,  $N_z$  and  $H_z$  are the grid parameters as defined in Sect. 3.1. Both low and high resolution double grids have  $M_z = 6$ ,  $R_{\max} = 50$  kpc,  $z_{\max}^A = 3.6$  kpc and  $z_{\max}^B = 21.6$  kpc. # is the number of particles,  $c_s$  the sound speed of the gas,  $t_o$  the gas switch-on time and  $t_{\text{end}}$  the time to which the simulation is performed. The points refer to the former lines.

Simulation	$N_R$	$N_\phi$	$N_z$	$H_z$ [pc]	# NS	# disc	# DH	# gas	$t_o$ [Myr]	$t_{\text{end}}$ [Myr]	$c_s$ [km s $^{-1}$ ]
sxx	32	32	73	100	83 444	178 022	225 284	0	–	5000	–
s10	.	.	.	.	.	.	.	20 000	3200	.	10
lxx	62	64	121	60	625 828	1 335 167	1 689 629	0	–	.	–
l10	.	.	.	.	.	.	.	150 000	1800	2275	10
l20	.	.	.	.	.	.	.	.	.	.	20
l10'	.	.	.	.	.	.	.	.	2400	2775	10

(i) a ratio of disc over NS mass of 0.8 within the spheroidal volume  $s < 3$  kpc (where  $s^2 = R^2 + z^2/e^2$  and  $e = 0.5$ ), (ii) a total NS+disc mass of  $2.4 \times 10^{10} M_\odot$  in the same volume and (iii) a circular velocity of  $190 \text{ km s}^{-1}$  just after the very steep central rise of the rotation curve, taking into account the velocity scales adjusted to the observed stellar velocity dispersion in Baade’s window (see Table 3 of paper I). The DH parameters,  $a$  and  $h_z$  are fixed as in the reference simulation m00, and the other parameters are adjusted to the former constraints and to a disc surface density on the solar circle of  $60 M_\odot \text{ pc}^{-2}$ , yielding  $M_{\text{NS}} = 2.48 \times 10^{10} M_\odot$ ,  $M_{\text{d}} = 4.6 \times 10^{10} M_\odot$  and  $h_R = 3.2$  kpc. The mass density is softly truncated as in paper I, at radius  $R_c = 38$  kpc and over a width  $\delta = 5$  kpc, and the initial kinematics rests on the same relations between the velocity moments as in simulations m00-m10, except that the asymptotic velocity anisotropy  $\beta_\infty = 0.68$  and the transition radius  $r_o = 5.3$  kpc for the NS component.

## 5. Time evolution

Table 1 gives an overview of the simulations described in this paper. Two series of simulations have been realised: the first one with moderate number of particles and spatial resolution (series “s”, small simulations), and the other one pushing these quantities such as to exploit about half of the memory resources of the most powerful computers available at Geneva University (series “l”, large simulations). In each series, we first integrated the initial axisymmetric model for 5 Gyr keeping the gaseous component fixed (simulations “xx”), and then we relaxed the gas particles at different intermediate times  $t_o$ . The gas is not evolved from the beginning because the non-inclusion of star formation produces an excessive accumulation of gas in the central region due to the torques of the non-axisymmetric gravitational potential, raising the rotation curve and leading to a premature destruction of the bar (Friedli & Benz 1993) or even preventing its formation. Instead of introducing an artificial gas recycling procedure, the time consuming gas-live simulations of the l-series were integrated only over a few 100 Myr. To damp the initial disequilibrium of the gas owing to its circular kinematics in the already barred potential, the non-axisymmetric part of the potential is progressively and lin-

early brought to its nominal value in 75 Myr, i.e. roughly half a rotation period of the bar.

In the l-series, the gas has been released at two different times after the formation of the bar, at  $t_o = 1.8$  and 2.4 Gyr. In the first case, two values of the sound speed have been explored,  $c_s = 10$  and  $20 \text{ km s}^{-1}$  (simulations l10 and l20 respectively), and in the second case only  $c_s = 10 \text{ km s}^{-1}$  has been retained (simulation l10'). In the s-series, many runs with live gas have been performed, releasing the gas every 400 Myr and each time with two different sound speeds, but only the one mentioned in Table 1 will be discussed here. The adiabatic index of the gas is set to that of neutral hydrogen, i.e.  $\gamma = 5/3$ . Taking the vertical gravitational resolution  $H_z$  as a lower physical limit for the SPH smoothing length, the maximum gaseous density that can be reasonably modelised in the l-simulations is  $\sim W(0, H_z) \cdot N_o/N_g \cdot M_g \approx 2 M_\odot \text{ pc}^{-3}$  (see the previous sections for the meaning of the symbols), which is at least one order of magnitude below the density of the Galactic molecular gas, but sufficient to describe the warmer neutral phase with a typical sound speed of  $10 \text{ km s}^{-1}$ . However, Cowie (1980) has argued that a system of molecular clouds may be treated as a classical fluid with a sound speed equal to the mass averaged cloud velocity dispersion, which also amounts to  $10\text{--}20 \text{ km s}^{-1}$  in the Milky Way. Hence our simulations are expected to display properties of both the HI and H $_2$  medium.

The SPH particles all have the same time-independent mass. The number of particles in each luminous component is always such that the mass per particle is the same as for the gas component to minimise relaxation effects, and the number of DH particles corresponds to a mass per particle three times larger than for the other components. The typical number of SPH particles within  $R = 8$  kpc (in initial units) and the corotation circle in the high resolution simulations is  $10^5$  and  $5.5 \times 10^4$  respectively.

The simulations are run in a completely self-consistent way, without imposing any symmetry and taking into account all gravitational interactions between the mass components. In particular, the gas feels his own gravity and interacts with the stellar spiral arms. Moreover the bar parameters are not arbitrarily chosen but automatically and naturally adjust according to realistic dynamical constraints. The calculations have been

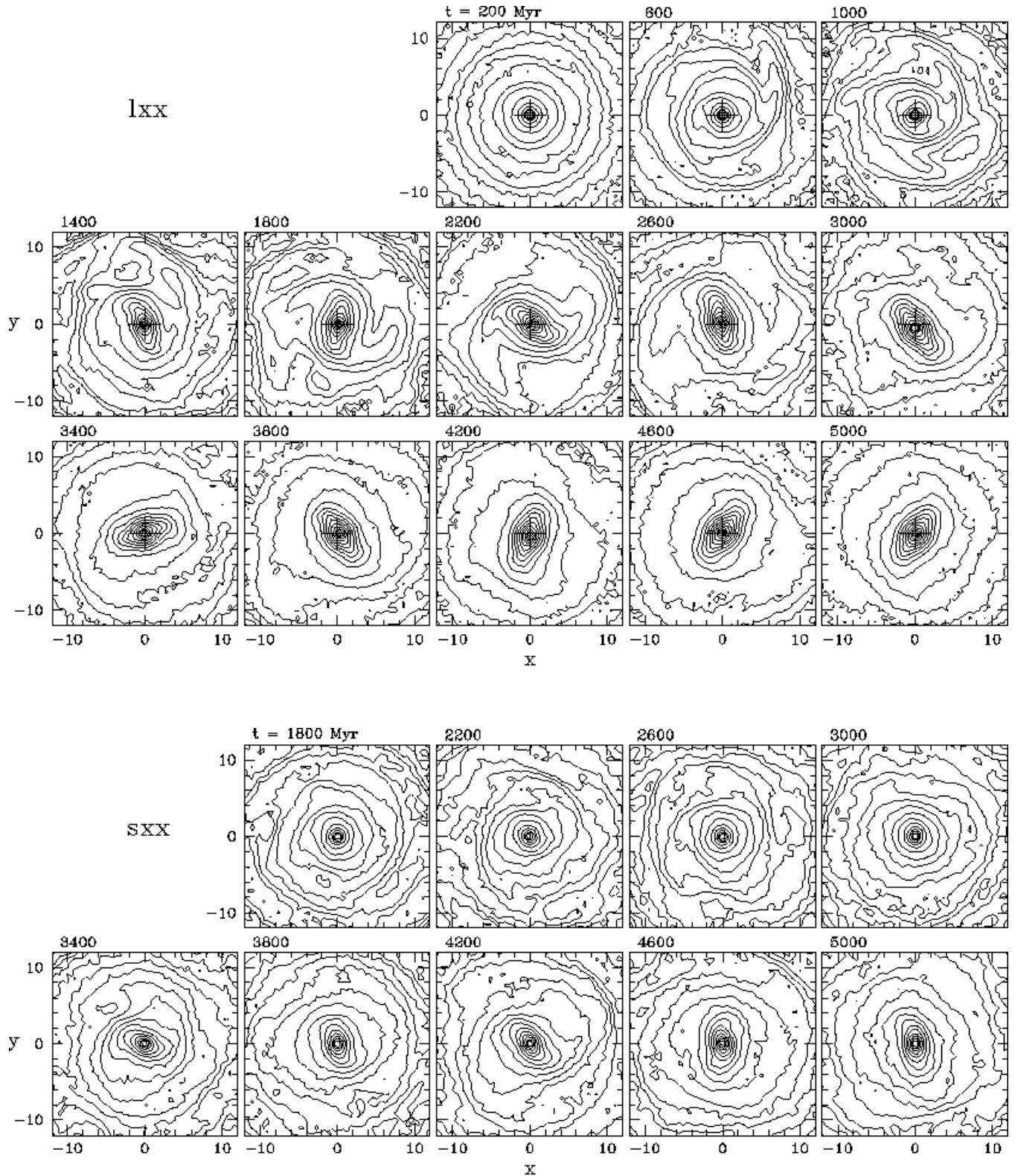


**Fig. 8.** Time evolution of the face-on disc+NS surface density in simulations  $lxx$  and  $sxx$  with fixed gas component. The distances are in kpc (initial units) and the density contours are spaced by a constant interval of 0.5 magnitude. The cross in the  $lxx$  frames indicates the position of the centre of mass, which coincides with the origin of the coordinates system.

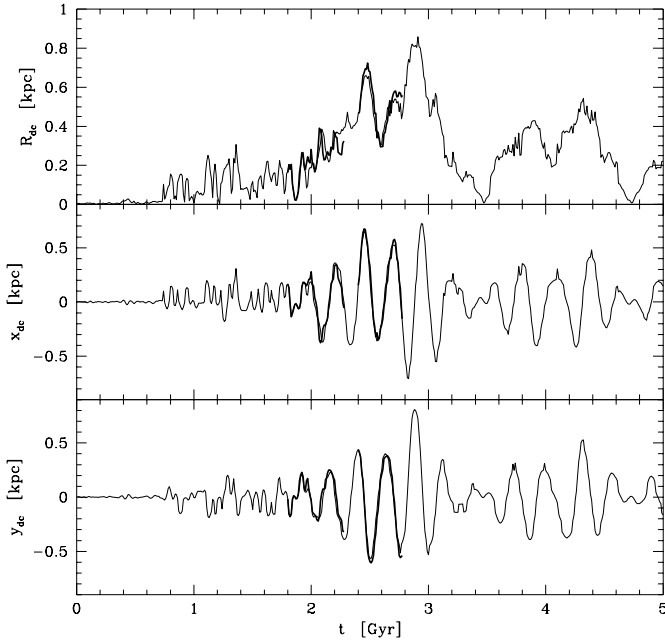


**Fig. 9.** Radial,  $x$ - and  $y$ -displacements of the stellar density centre (dc) with respect to the centre of mass in simulation lxx (thin line) and in the live gas simulations 110 and 110' (thick lines).

done on Sparc Ultra and Silicon Graphics computers, each with over 1 Gbyte central memory.

### 5.1. Stars

Figure 8 shows the whole face-on evolution of the simulations lxx and sxx with rigid gas component. Although the initial conditions of these simulations are drawn from exactly the same phase-space density function and the average number of particles per grid cell is about the same, the evolution clearly depends on the adopted resolution and number of particles: in simulation lxx the bar forms much more rapidly than in simulation sxx, around  $t = 1.2$  Gyr instead of 3.2 Gyr in the latter, and is of larger extent. Moreover, the contours of the bar become rounder close to the centre, as observed in many external barred galaxies (e.g. M100 in the near-IR), and the surrounding disc tends to a more flattened radial profile. An explanation for the delay of the bar formation could be that higher resolution simulations can catch smaller density fluctuations and hence favour the growth rate of asymmetries. It is not clear whether a convergence of properties with increasing resolution has been achieved in simulation lxx.

Another relevant dynamical aspect distinguishing the large simulations from those of the s-series is the offcentring of the stellar bar (Fig. 9). At  $t \approx 800$  Myr, the density centre starts to deviate from the global centre of mass and wanders around it. The maximum amplitude of the displacement reaches  $\sim 800$  pc at  $t = 2.9$  Gyr, and the revolution frequency of the density centre amounts to  $20 - 30 \text{ km s}^{-1} \text{ kpc}^{-1}$ . Offcentred bars are commonly observed in external galaxies (see Colin & Athanassoula

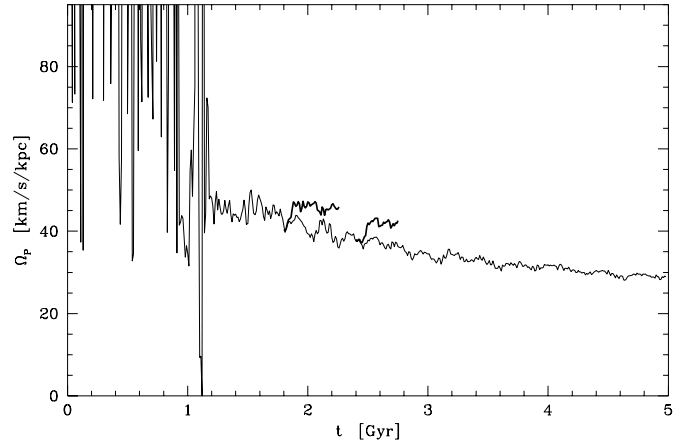


**Fig. 10.** Pattern speed  $\Omega_P(t)$  of the bar in simulation lxx with fixed gas (thin line) and in simulations 110 and 110' with live gas (thick lines), in initial units. The pattern speed is derived as in paper I by diagonalisation of the momentum of inertia tensor, except that the latter is computed relative to the offcentred density centre instead of the centre of mass.

1989; Block et al. 1994; other references in Levine & Sparke 1998) and reported in numerical simulations of galactic discs (e.g. Miller & Smith 1992). At least half of all spiral galaxies have lopsided light distribution (Schoenmakers 1999; see also Rudnick & Rix 1998). Figure 9 confirms Weinberg's (1994) conclusion on the persistent nature of the phenomenon. However, it might be that the polar grids used to compute the gravitational forces amplify the density centre offcentring, as they artificially produce an exponential instability of the position of the centre of mass (Pfenniger & Friedli 1993). The same simulation repeated with a three-dimensional Cartesian grid could result in a lower amplitude oscillation.

The pattern speed of the bar in simulation lxx decreases roughly exponentially from  $50 \text{ km s}^{-1} \text{ kpc}^{-1}$  at  $t = 1.2$  Gyr to  $30 \text{ km s}^{-1} \text{ kpc}^{-1}$  at  $t = 5$  Gyr (see Fig. 10). The face-on axis ratio  $b/a$  of the bar is about 0.6, i.e. close to the upper limit derived from the lower resolution simulations of paper I.

The phase space coordinates of the stellar particles have been extracted from the simulations every 25 Myr. Adjusting the location of the observer (Sun) using the COBE/DIRBE dust subtracted K-band map as in paper I is complicated by the density centre offcentring: in addition to the bar inclination angle, the relative galactocentric distance of the observer and the mass-to-light ratio, further parameters are needed for the direction of the Galactic centre in the models. Here we have simply applied the standard method of paper I to models with weakly offcentred bars, assuming that the Galactic centre lies at the centre of mass and taking a finer Cartesian grid with  $\Delta\ell = \Delta b = 0.5^\circ$  to compare the data and model fluxes. In the notations of paper I (see also Sect. 6) and for  $N_{\text{pix}} = 1200$ , the best fit location parameters for model lxx1950 are  $\tilde{R}_o = 9.7$  and  $\varphi_o = 32^\circ$ , with a mean quadratic relative residual  $\mathcal{R}^2 = 0.539\%$ . A comparison of this model to the COBE data is shown in Fig. 11.

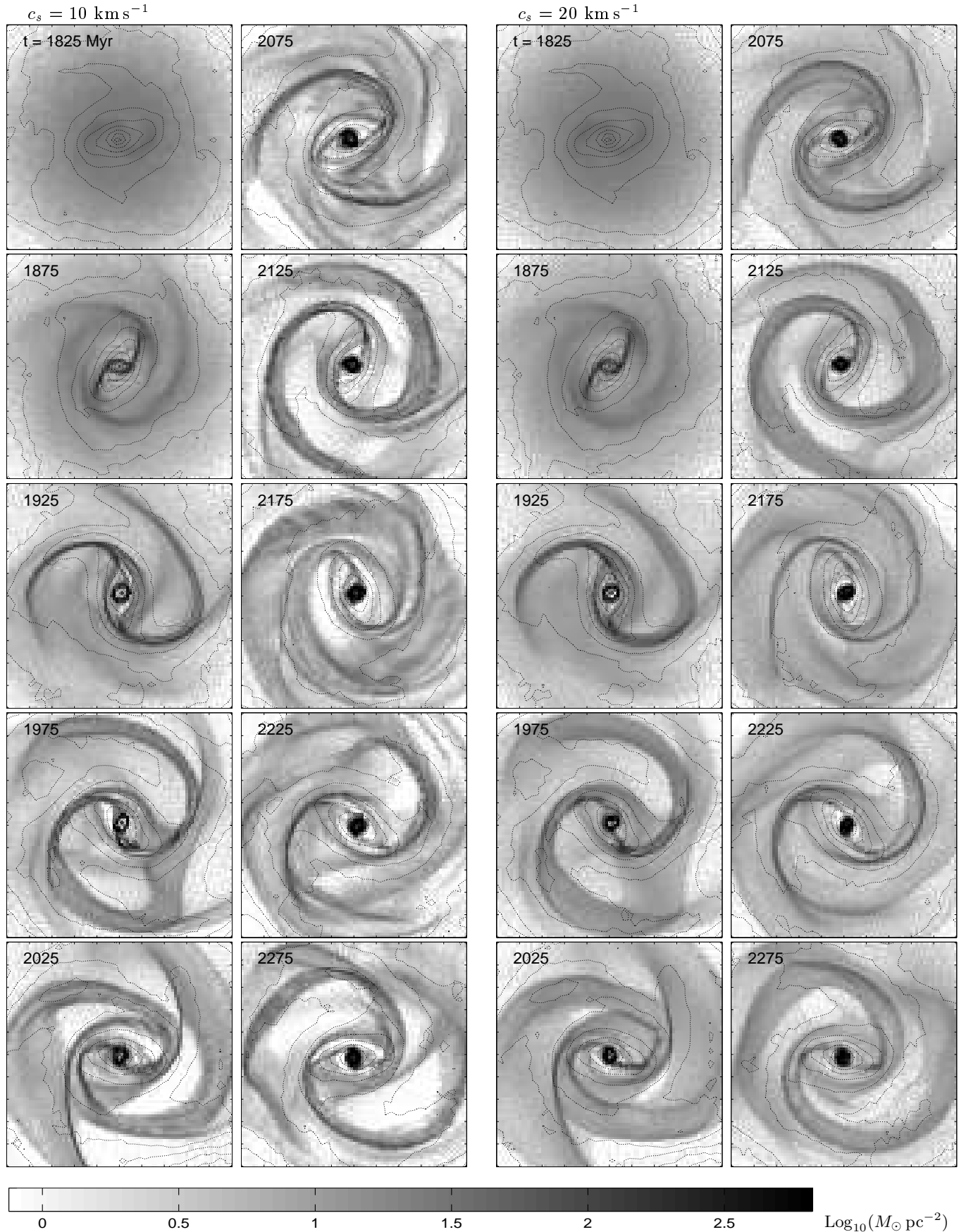


**Fig. 12.** Face-on view of the gas flow evolution in simulations 110 and 120, which differ only by the value of the sound speed  $c_s$ . Each frame is 20 kpc on a side in initial units. The dotted lines indicate the stellar surface mass density contours spaced by 0.75 magnitude.

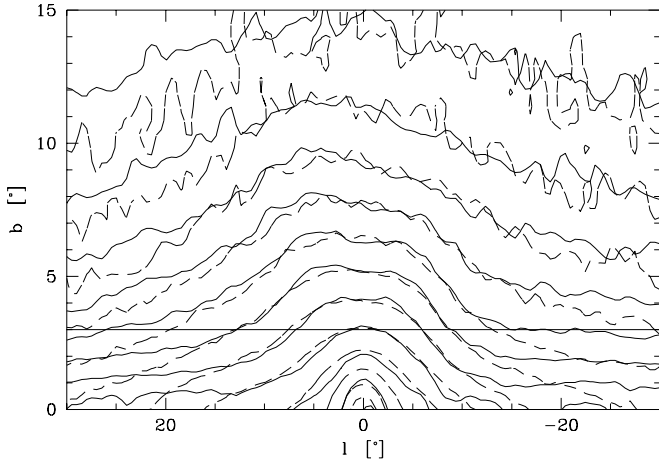


**Fig. 11.** Result of an adjustment of model lxxt1950 to the dust subtracted COBE K-band image by the same technique as described in paper I. The solid lines show the observed contours spaced by half a magnitude and the dashed lines the corresponding model contours, assuming a constant mass-to-light ratio. The correction for extinction fails below the horizontal line.

### 5.2. Gas

The time evolution of the gas flow in simulations 110, 120 and 110' is illustrated in Figs. 12 and 13. In each simulation the gas flow rapidly becomes non-axisymmetric, forming transient spiral arms, shock fronts and a nuclear ring of  $x_2$  orbits accumulated near the inner Lindblad resonance. Two kinds of spiral structure can a priori be distinguished in the bar region (see for instance frame  $t = 2075$  Myr of simulation 110 in Fig. 12 or frame  $t = 2775$  Myr in Fig. 13):

- The *axis shocks*, or *off-axis shocks*, which lead more or less the bar major axis and join the nuclear ring. These shocks, also appearing in many other hydrodynamical simulations (e.g. Athanassoula 1992), can be roughly understood on the basis of the  $x_1$  closed orbit family in the rotating frame of the bar (Binney et al. 1991; Morris & Serabyn 1996), under the approximation of a rigid potential. Far from the centre, the gas moves along this main orbit family because the viscous forces dissipate any libration energy around periodic orbits. The same forces also cause the gas to switch progressively to ever lower energy orbits and thus to approach the centre. Below a critical value of the Hamiltonian, the  $x_1$  orbits develop loops at their apocentre where the gas dissipates some of its streaming energy by collision. The gas then leaves these periodic orbits to follow more radial non-periodic orbits passing round the nuclear ring and striking the gas falling symmetrically from the other side of the bar. The axis shocks result from the velocity difference between the two streams, when it exceeds the sound speed. Part of the falling gas may also collide with the central  $x_2$  orbits and be directly absorbed by the nuclear ring. Axis shocks have been detected in the velocity field of several external

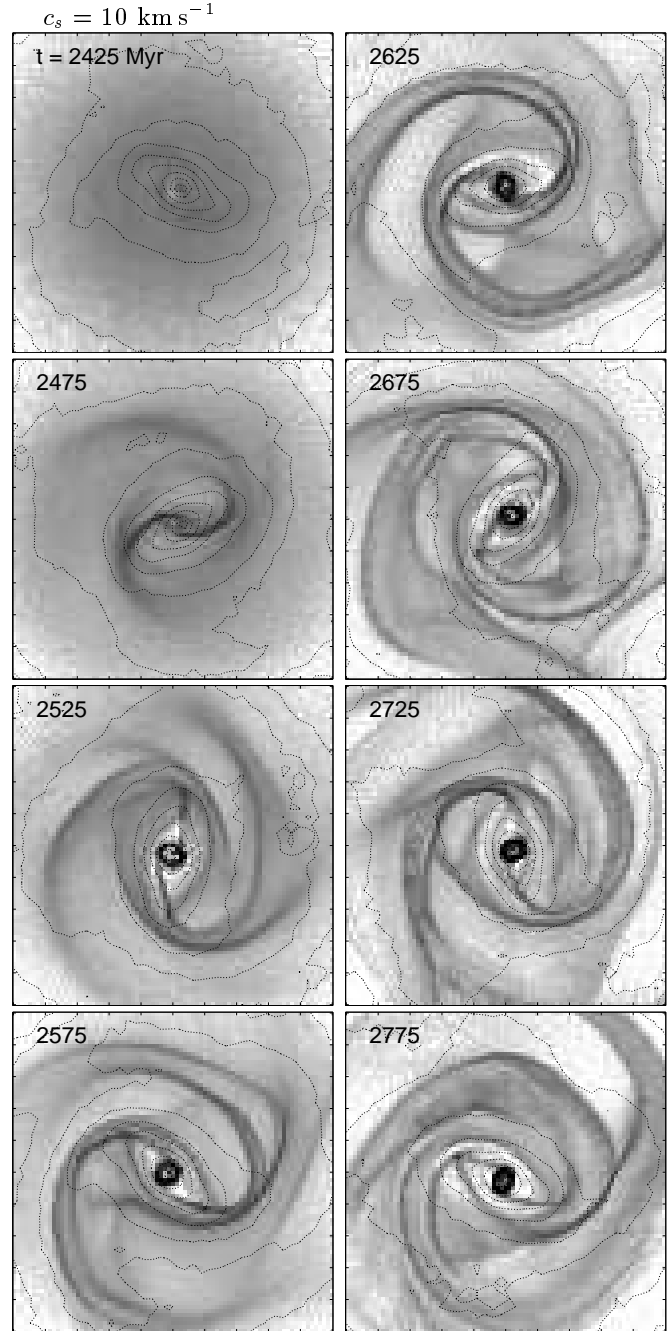


**Fig. 13.** Face-on view of the gas flow evolution in simulation 110'. Each frame is 20 kpc on a side in initial units. The gray scale and the dotted contours are as in Fig 12.

barred galaxies (see Sect. 6.3) and seem to be associated with the prominent dustlanes leading the bar in these galaxies. The dust grains are strongly concentrated behind the shock fronts and thus produce the typical extinction signatures. Some prototypical galaxies with offset dustlanes are NGC 1300, NGC 1433, NGC 1512, NGC 1530, NGC 1365 and NGC 6951, which are all SBb or SBbc type galaxies (see e.g. Sandage & Bedke 1988), as the Milky Way. The

self-gravity of the gas certainly plays an important role in holding together the shocked gas.

- The *lateral arms*, which roughly link the bar ends avoiding the nuclear ring by a large bow, and generally correspond to the inner prolongation of spiral arms in the disc. The gas moves almost parallel to these arms and finally meets the axis shocks. According to Mulder & Liem (1986), the 3-kpc arm is almost certainly of this kind. When a lateral arm forms, the part close to the axis shock where the gas runs into is located well inside the bar. Then the arm moves outwards along the axis shock and progressively dissolves as it approaches corotation (this will be illustrated more quantitatively in Sect. 7). Such dissolution may be partly linked with the decreasing gravitational resolution with radius in the simulations. The gaseous lateral arms in our simulations resemble the innermost, sometimes ring-like, stellar arms in external barred galaxies, e.g. NGC 1433, NGC 4593, NGC 6951, NGC 3485, NGC 5921, NGC 7421, which are also SBb or SBbc type galaxies (Sandage & Bedke 1988).

lateral arms pass away from it.

Increasing the sound speed, i.e. the pressure forces relative to the gravitational forces, yields as expected a smoother gas distribution and softens the sharp corners in the spiral arms (see Fig. 12). The nuclear ring slightly shrinks and the axis shocks occur closer to the major axis of the bar, in agreement with the SPH results of Englmaier & Gerhard (1997). Note that some sub-structures also seem to develop within the nuclear ring for  $c_s = 20 \text{ km s}^{-1}$ .

The gas flow never reaches a stationary state and is most of the time asymmetric, as is often observed in external disc galaxies. In particular, the lateral arms are rarely symmetric both in position and surface density, and the axis shocks considerably vary in shape. Sometimes, only one lateral arm or axis shock can be distinguished, and sometimes these structures are doubled, appearing twice on the same side of the bar (see e.g. 110t2175 in Fig. 12 for double lateral arms). It may even happen, as is the case in frame  $t = 1975 \text{ Myr}$  of simulation 110 (Fig. 12), that the axis shocks receive a sufficient impulse from the lateral arms to transform themselves into such arms. The nuclear ring, owing to its gravitational coupling to the stellar components, intimately follows the bar density centre in its oscillations around the centre of mass. The inclusion of gas prevents the pattern speed of the bar to slow down (Fig. 10; see also Friedli & Benz 1993; Berentzen et al. 1998): after a substantial initial readjustment,  $\Omega_P$  remains very nearly constant over the short duration of the live gas simulations.

In the *s*-series, the moderate bar considerably weakens once the gas is switched-on. However, in simulation s10 it survives for a sufficiently long time to reveal an interesting asymmetric process in the gas flow (Fig. 14): the gas seems to rarefy alternately on each side of the bar intermediate axis according to a cycle of roughly 125 Myr. As a large amount of gas flows on one side, the other appears almost devoided of gas, and when the gas of the former side reaches the axis shock, the situation reverses and the previously depleted side is filled. During this cycle, the gas density on the bar flanks can vary from single to triple.

The non-stationarity of the gas flow in the *l*-simulations is not a simple unachieved readjustment due to non-equilibrium in the initial conditions and the rather short integration time, since the smaller simulations with live gas, integrated much longer in time, themselves always remain time-dependent. Outside the bar region, the stellar spiral arms have a differential pattern speed, in general lower than the bar (see e.g. Sellwood & Sparke 1988), and drive the gaseous arms which repeatedly wound and dissolve. Many SPH simulations carried in rigid barred potentials seem to finally settle in a stationary spiral structure rotating at the same angular speed as the bar. Such results are an artificial consequence of the imposed fixed background potential.

## 6. Interpretation of the $\ell - V$ features

Model  $\ell - V$  diagrams depend on the location of the observer in the galactic plane, which is described by his galactocentric

This classification should only be considered as a first order guide. The main distinction between the two structures is that the axis shocks intersect or brush the nuclear ring, while the

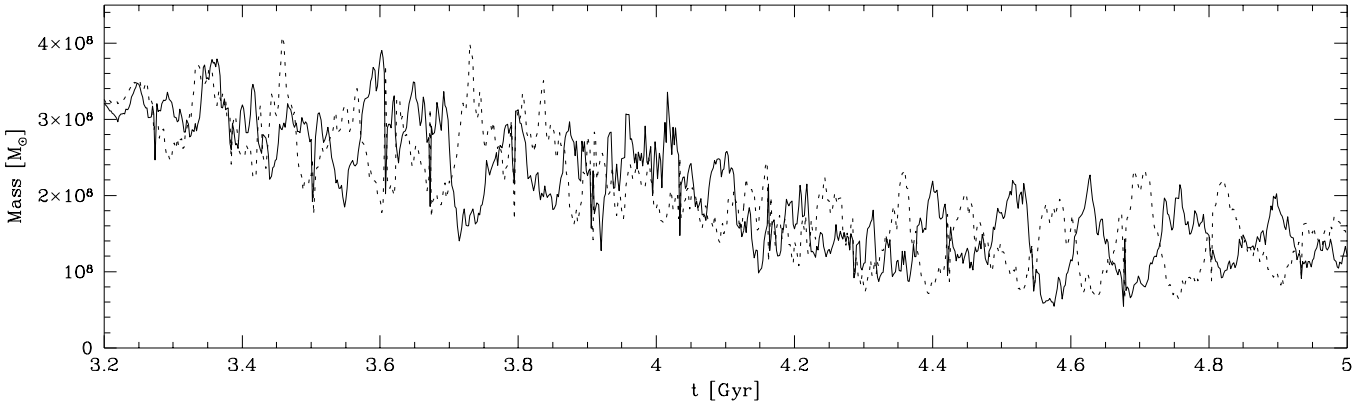


**Fig. 14.** Asymmetric alternated cycle of the gas flow on the bar flanks in the small simulation s10. The full and dotted lines indicate the gas mass inside each of the two regions corotating with the bar, located within 3 kpc from the centre and at least 500 pc away from the bar major axis. The cycle is especially marked in the last 700 Myr of the simulation (in which the bar never gets significantly offcentred).

**Table 2.** Reference points overlaid in the  $\ell - V$  diagram movies to locate the main observed features indicated in Fig. 1 and the Carina arm.

Reference	$\ell$ [ $^\circ$ ]	$V$ [ $\text{km s}^{-1}$ ]
Positive bright velocity peak	3	270
Negative bright velocity peak	-2	-220
Intersection of the 3-kpc arm with the $\ell$ -axis	12	0
Knee of the 3-kpc arm	-17	-125
Knee of the $135\text{-km s}^{-1}$ arm (Clump 1)	-5	100
Maximum emission of the connecting arm	7.5	150
Tangent points of the molecular ring branches	25	120
	30	115
Tangent point of the Carina arm	-78	0

distance  $\tilde{R}_o$  in initial units and the angle  $\varphi_o$  between the line joining himself to the centre and the major axis of the bar, and on his velocity  $v_o$ . We assume here that the observer lies in the plane  $z = 0$  and that  $v_o$  is purely azimuthal.

The phase space coordinates of the SPH particles have been stored every 2 Myr in order to realise a posteriori  $\ell - V$  diagram movies for any arbitrary values of these parameters with a high temporal resolution. To compare these movies with the observations and decide for an optimum model, some reference points have been overlaid on the movies to localise the features seen in the CO and HI data (Table 2). In each movie, the view point is at rest relative to the rotating frame of the bar, i.e.  $\tilde{R}_o$  and  $\varphi_o$  remain constant. The contribution of each SPH particle to the  $\ell - V$  frames is weighted by its inverse squared distance relative to the observer to mimic the flux decline of point sources (all model  $\ell - V$  diagrams in this paper are computed this way, except the one in Fig. 21). A direct consequence of the asymmetries developing in our simulations is that model  $\ell - V$  diagrams computed for diametrically opposite view points always considerably differ.

Two models from these movies, 110t2066 and 110't2540, illustrated and confronted to the observations in Fig. 15, have especially retained our attention. In both cases, the inclination angle of the bar is  $25^\circ$  and no velocity rescaling has been applied. The circular velocity of the observer is set to the mean azimuthal velocity of his surrounding SPH particles, i.e. to  $203 \text{ km s}^{-1}$  for 110t2066 and  $197 \text{ km s}^{-1}$  for 110't2540. The model 110't2540 is selected as one of the models which best reproduce the overall  $\ell - V$  observations within the solar circle. Even if the agreement is rather qualitative, this model offers a solid basis to interpret the data. Figure 16 highlights the spiral arms which trace the  $\ell - V$  features in the model and Fig. 17 shows the velocity field of the gas. Figure 18 also provides a qualitative key-map to spatially locate observed  $\ell - V$  sources in the Galactic plane.

### 6.1. Connecting arm

The connecting arm is clearly identified with the axis shock in the near part of the bar. More precisely, this arm is build up by the gas clouds which have recently crossed the shock front at various galactocentric distances and which now collectively plunge towards the nuclear ring/disc with velocities roughly parallel to the shock front. In other words, the connecting arm traces the near-side branch of the Milky Way's dustlanes. Other models, like 110t2066 in Fig. 15, exhibit axis shocks with  $\ell - V$  traces resembling much more the real connecting arm than in model 110't2540, thus reinforcing our interpretation.

The presence of the connecting arm feature in the observed  $\ell - V$  diagrams can be considered as a further evidence of the Galactic bar. Furthermore, its rather large domain in longitude is relevant of an extended bar, especially if the latter is seen close from its major axis (see Sect. 7). The connecting arm feature is a real concentration of gas in space and not an artifact due to velocity crowding along the line of sight, as suggested

by Mulder & Liem (1986)<sup>1</sup>. In our simulations, the gas does not always trace the full length of the axis shocks and hence it is not surprising that the emission from the connecting arm appears truncated at  $\ell \gtrsim 10^\circ$ . The  $\ell - V$  movies sometimes show gas lumps deposited by lateral arms in the near-side axis shock and moving precisely along the connecting arm feature. The time for the gas to travel from the endpoint of a lateral arm to the nuclear ring along the shock is of order 15 – 20 Myr and it takes about another 10 Myr for the gas not absorbed by the ring to encounter the opposite axis shock. The fraction of gas deposited in the nuclear ring is time-dependent, but has been estimated to 20% in a steady gas flow model of NGC 1530 (Regan et al. 1997). The gas mass in each branch of the axis shocks is  $\sim 4 \times 10^7 M_\odot$  or less.

According to Fig. 16, the axis shock in the far-side of the bar is predicted as an almost vertical feature in the  $\ell - V$  diagram, i.e. with  $\ell \approx \text{constant}$ . Such a feature is indeed visible in the  $^{12}\text{CO}$  observations (Fig. 1) near  $\ell = -4^\circ$ , with only a marginal decrease of absolute longitude towards negative velocities. The longitude confinement comes from the fact that the shock line is nearly parallel to the line of sight and the velocity extension from the fact that the velocity of the gas along the shock rapidly increases when approaching the nuclear ring/disc.

### 6.2. 3-kpc and 135-km s<sup>-1</sup> arms

The 3-kpc and the 135-km s<sup>-1</sup> arms are lateral arms. The observed velocity asymmetry between these two arms happens because the latter passes closer to the centre than the former. The gas associated with the 135-km s<sup>-1</sup> arm, moving almost parallel to the arm (Fig. 17), indeed falls deeper in the potential well of the nucleus and therefore reaches higher forbidden velocities before striking the dustlane shock.

The observed velocity asymmetry of bright emission near the positive and negative terminal velocity peaks could have a related origin: the gas from the 3-kpc arm, after crossing the dustlane shock further out than its counterarm, starts to fall towards the nuclear ring/disc with a higher potential energy and therefore will approach the latter with higher velocities, producing an enhanced velocity peak. Model 110't2540 however does not exhibit such a velocity asymmetry. This asymmetry could also arise from a relative radial motion between the nuclear ring/disc and the LSR, produced either by the oscillations of the density centre (see Sect. 5.1) or by a radial velocity component of the LSR with respect to the Galactic centre, possibly induced by the bar itself (Raboud et al. 1998), or both.

The inner branch of the molecular ring, with tangent point at  $\ell \approx 25^\circ$ , is the outer extension of the 135-km s<sup>-1</sup> arm.

<sup>1</sup> These authors pretend that the connecting arm intervene between longitudes  $10^\circ$  and  $20^\circ$ , which obviously conflicts with the sources (van der Kruit 1970 and Cohen 1975) they mention.

### 6.3. Bania's clumps

Observations of the gas velocity field in external barred galaxies have revealed velocity changes up to 200 km s<sup>-1</sup> across the bar leading dustlanes, demonstrating that these dustlanes are associated with very strong shocks. Such velocity fields have been measured for example in NGC 6221 (Pence & Blackman 1984), NGC 1365 (Joersaeter & van Moorsel 1995; Lindblad et al. 1996), NGC 3095 (Weiner et al. 1993), NGC 1530 (Regan et al. 1997; Reynaud & Downes 1998) and NGC 7479 (Laine et al. 1999). Figure 19 shows how the gas velocity field is affected by the near-side branch of the axis shocks in model 110t2066.

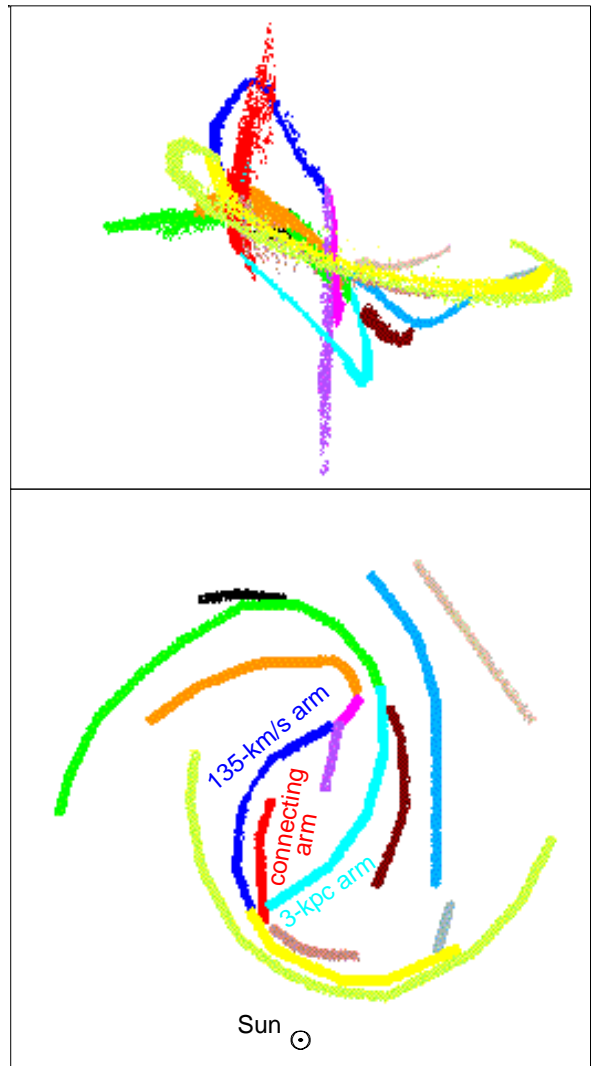


**Fig. 16.** Link between the spiral arms in the  $x - y$  plane and the  $\ell - V$  features in model 110't2540. The spiral arms and their  $\ell - V$  traces are depicted by the true phase space coordinates of the gas particles, using all particles within a narrow band of 300 pc centred on the maximum surface density curve of each spiral arm. In the upper plot, closer structures relative to the observer have been overlayed on the more distant ones. The nuclear ring is not represented.



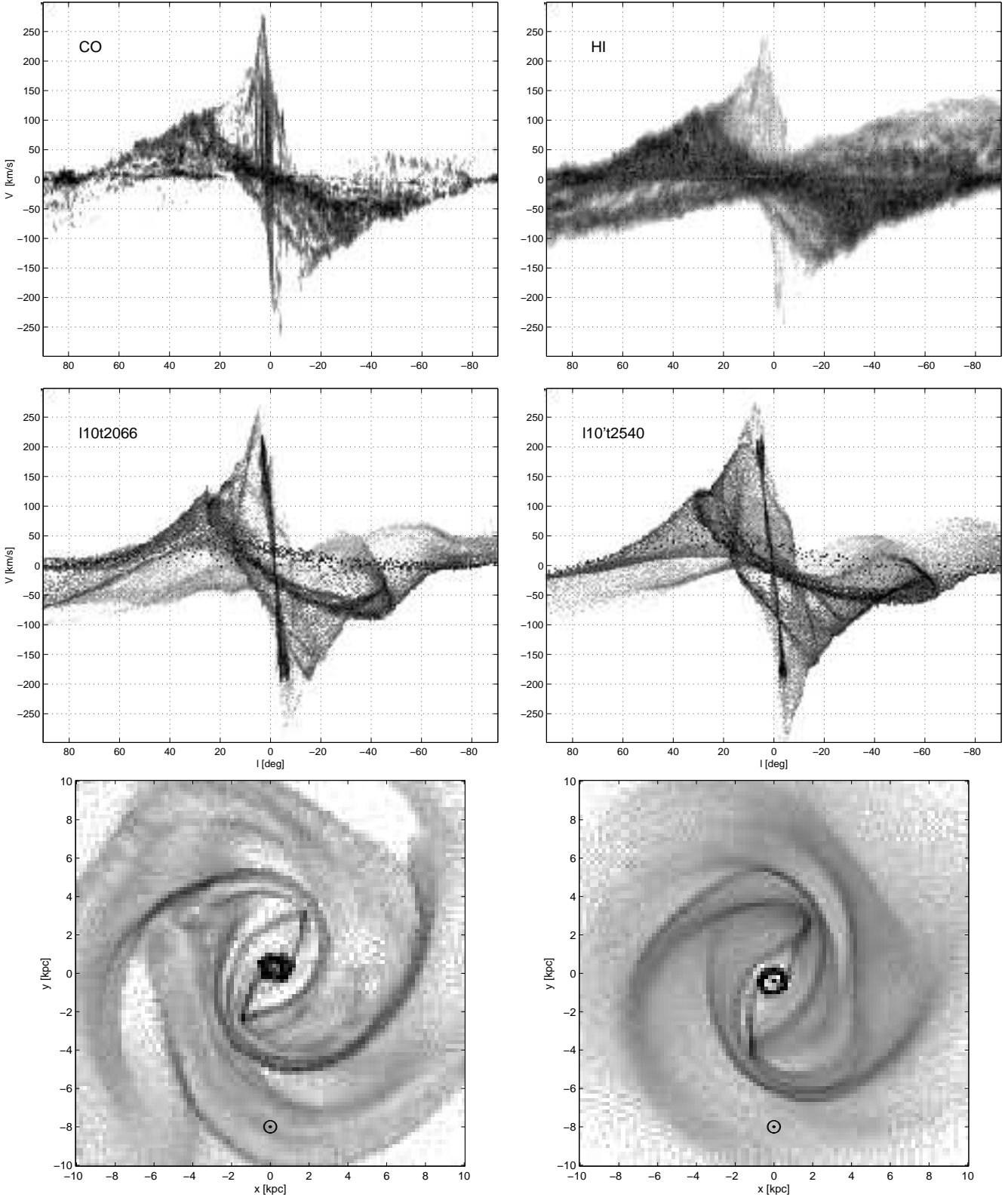


**Fig. 15.** Confrontation of a selection of two models with observed gas kinematics. Top:  $^{12}\text{CO}$  and HI  $\ell - V$  diagrams integrated over  $|b| \leq 2^\circ$  and  $|b| < 1.25^\circ$  respectively; the data are from Dame et al. (1999) for the CO, and Hartmann & Burton (1997), Burton & Liszt (1978) and Kerr et al. (1986) for the HI. Middle: synthetic  $\ell - V$  diagrams of models 110t2066 and 110't2540 for a bar inclination angle  $\varphi_o = 25^\circ$ , including all particles within  $|b| < 2^\circ$ . Bottom: face-on projections of the gas spatial distribution in these models, rescaled such as to put the observer at  $(x, y) = (0, -8)$  kpc ( $\odot$  symbol). In these units, corotation lies at  $R_L = 4.5$  kpc (110t2066) and 4.4 kpc (110't2540). The model on the left reproduces almost perfectly the connecting arm, while the model on the right provides a fair global qualitative agreement to the data.

The shock occurs near  $x = -0.55$  kpc and is followed downstream by a huge gas concentration. Both velocity components, parallel and perpendicular to the shock front, undergo an abrupt velocity gradient across the shock layer. The velocity change is however larger for the parallel component, reflecting the shearing nature of the axis shocks, and is comparable to the values observed in external galaxies. In NGC 1530, Reynaud & Downes (1998) found that the velocity change increases towards the nuclear ring, but this property is hard to infer from our models because the shock fronts are not well resolved in the low density part.

Bania's (1977) clump 2 and an other vertical feature near  $\ell \approx 5.5^\circ$  (see Fig. 1) could represent gas lumps which are just about to cross the near-side dustlane shock somewhere between the 3-kpc arm and the nuclear ring/disc: the upstream part still moves with the small quasi-apocentric velocities of the pre-shock orbits, while the downstream part has been accelerated to the high inwards post-shock velocities, giving rise to a steep radial velocity gradient (Fig. 18) and a velocity stretch of over  $100 \text{ km s}^{-1}$  in the observations. Contrary to the  $\ell - V$  trace of the far-side dustlane shock, these features might be really concentrated in space and not result from an accumulation of gas along the line of sight. For the  $\ell = 5.5^\circ$  lump, this interpretation is supported by the fact that all emission from the lump originates at nearly constant latitude, as expected from a spatially confined source, and that the part of the connecting arm at the same longitude as the lump appears at almost the same latitude as the lump itself (see Fig. 2). Furthermore, this lump also has a small mass relative to the connecting arm and will

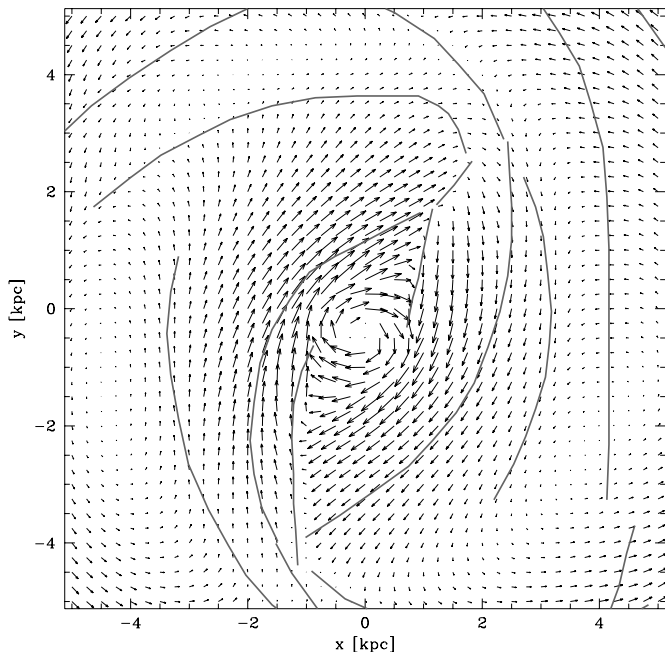


**Fig. 17.** Velocity field of model 110't2540 in the rotating frame of the bar. The subtracted solid rotation does not take into account the bar offcentring. The grey curves indicate the location of the spiral arms.

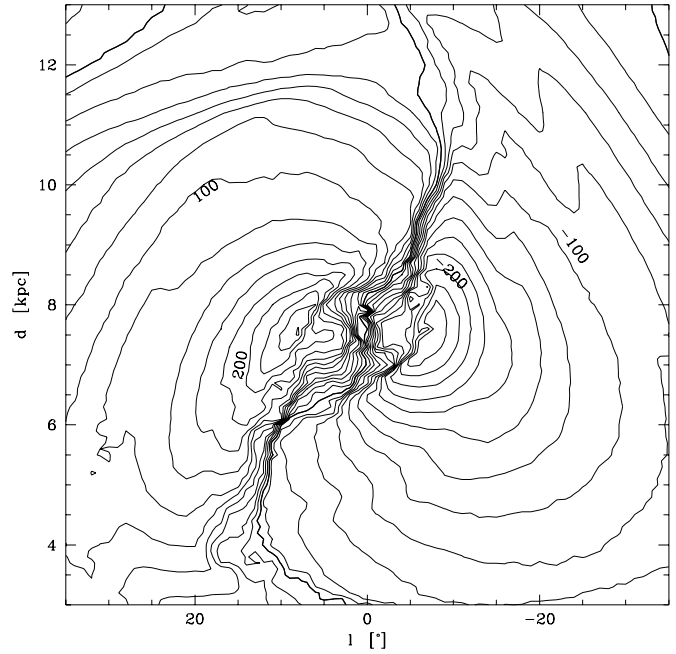


**Fig. 18.** Radial velocity contours in model 110't2540 as a function of longitude and distance relative to the observer, whose location and circular velocity are as in Fig. 15. The spacing of the contours is  $20 \text{ km s}^{-1}$  and the thick contour is the zero velocity curve (labels are given in  $\text{km s}^{-1}$ ). Only the particles within  $|b| < 2^\circ$  have been considered. Note the very sharp velocity gradient when crossing the axis shocks.

therefore essentially adapt its momentum to that of this arm. For clump 2, with a mean latitude differing by more than  $0.5^\circ$  from that of the connecting arm (at similar  $\ell$ ) and a total mass of nearly  $10^7 M_\odot$  (Stark & Bania 1986), our interpretation is more speculative. However, if this clump is indeed close to the apocentre of its orbit, it will enter very slowly the shock line, where gas is moving at very high speed (over  $200 \text{ km s}^{-1}$ ), and thus receive a significant impulse when integrated over time. Moreover, the clump complex may move on a kind of looped quasi- $x_1$  orbit and therefore will self-dissipate its energy if its size is comparable to that of the loops, whatever its mass. If the connecting arm indeed traces the near-side dustlane, the identification of clump 2 with such a dustlane, as proposed by Stark & Bania (1986), is ruled out (unless the Milky Way has a double bar). But it should be noted that the axis shock assigned to the connecting arm in model 110't2540 can produce an  $\ell - V$  trace resembling much more that of clump 2 if the bar inclination angle is reduced to  $15^\circ$  (see Fig. 22).

Clump 1, composed of several clouds which are not bound to each other (Bania et al. 1986), is the southern terminus part of the  $135\text{-km s}^{-1}$  arm which penetrates the far-side dustlane shock. According to model 110't2540, its dynamics should be rather subtle: a part of its gas is absorbed by the dustlane, resulting in a huge velocity change like those described above, from  $V \approx 100 \text{ km s}^{-1}$  to  $V \lesssim 0$ , and the other part, corresponding to the portion of clump 1 at  $\ell \lesssim -5^\circ$ , is gliding outwards along

but without crossing the shock front until apocentre is reached (see the magenta segment in Fig. 16). The momentum injected by this cloud into the axis shock gas bends the outer segment of the shock. Since the far-side dustlane is nearly aligned with the line of sight, the vertical feature near  $\ell = -4^\circ$  is in fact a superposition of dustlane gas moving along this line and of clouds with shock induced velocity gradients (see Fig. 20). Clump 1 must be a very perturbed and compressed region, and hence a potential site of star formation a priori. An indicator of “readiness” for star formation is given by the  $^{12}\text{CO } J = 2 \rightarrow 1$  to  $J = 1 \rightarrow 0$  ratio, tracing dense molecular clouds, which is indeed particularly high for this clump (Hasegawa 1997, private communication). However, the strong shearing in the shock may prevent any star formation to proceed (e.g. Reynaud & Downes 1998). The bulk of this clump, owing to its large mass and impact velocity, may also cross the shock front without being too much affected.

#### 6.4. Tilt of the gaseous disc

A further observational argument supporting our interpretation of the dominant  $\ell - V$  features is the fact that the connecting arm and the portion of the 3-kpc arm at positive longitude, located in the near-side of the bar according to the models, have their maximum emission below the Galactic plane (i.e. at  $b < 0$ ), and that the dustlane near  $\ell = -4^\circ$  and the negative longitude part of the 135-km s $^{-1}$  arm, located in the far-side of the bar, above this plane (i.e.  $b > 0$ ; see Fig. 2). Hence structures predicted to be spatially close to each other by the models are indeed found at similar latitude in the observations.

Consequently, the gaseous disc within the central 1 – 2 kpc is tilted relative to the plane  $b = 0$ . Referring to Fig. 2, emission of the connecting arm at  $\ell \approx 5^\circ$ , i.e. where  $b$  stops to decrease as  $\ell$  increases, occurs near  $b = -1^\circ$ . Approximating the dustlanes by a straight line across the Galactic centre with an in-plane inclination angle of  $\varphi_o = 25^\circ$  (see Sect. 7), the source of this emission is tilted by  $\theta = \tan^{-1} |\sin \varphi_o \tan b / \sin \ell| = 4.8^\circ$  out of the Galactic plane, corresponding to a distance of about 120 pc below this plane. Similarly, the far-side dustlane ends at  $\ell \approx -4.5^\circ$  with  $b \approx 0.8^\circ$ , implying a tilt  $\theta = 4.3^\circ$  and a height of  $\sim +135$  pc. A similar tilt is also apparent on the  $^{12}\text{CO}$  longitude-latitude map of Dame et al. (1987; 1999), where the dustlanes contribute only very little to the total emission. Blitz & Spergel (1991) have inferred an apparent  $5.5^\circ$  central tilt of the bar major axis from balloon  $2.4 \mu\text{m}$  observations of the Galactic bulge within  $|\ell| < 12^\circ$  and  $|b| < 10^\circ$ . However, such a tilt has not been confirmed by the more recent near-IR COBE/DIRBE maps (Weiland et al. 1994). In the dust subtracted K-band map (paper I), the latitude centroid as a function of longitude, excluding the high extinction zone  $|b| < 3^\circ$ , only shows a significant tilt when regions beyond  $10^\circ$  from the Galactic plane are included, but then the tilt is likely an artifact due to the growing contribution of zodiacal light. The small tilt angle derived here is not generated by a position of the Sun above the Galactic plane, which is only of order 10 – 40 pc (Humphreys & Larsen 1995 and references therein), and con-

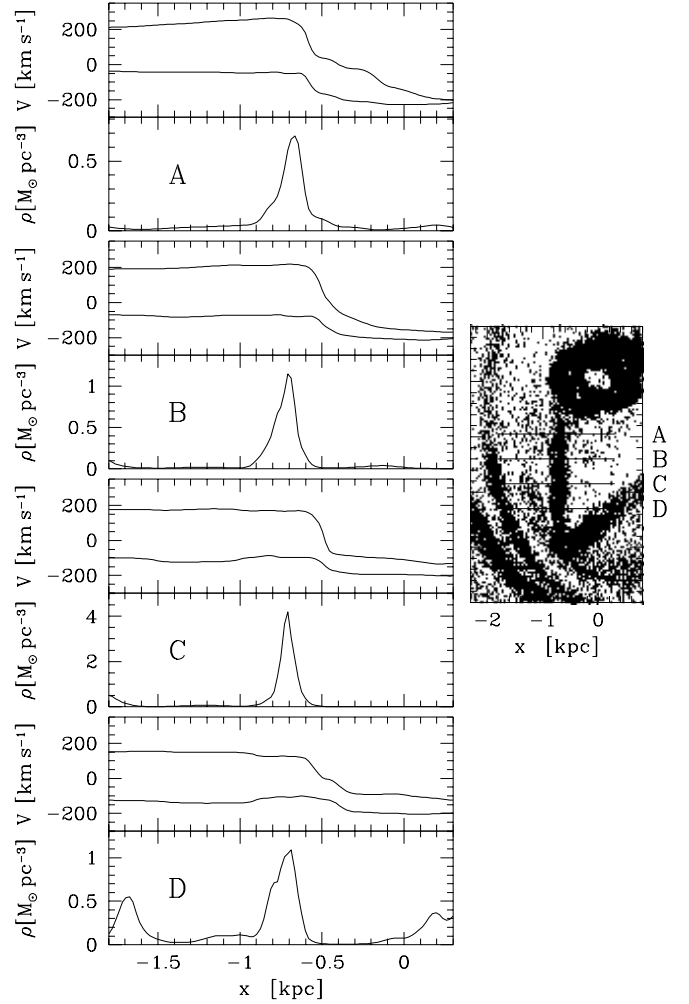


**Fig. 19.** Spatial density and velocity profiles along four slits perpendicular to the “connecting arm” in model 110t2066. The upper and lower velocity curves respectively stand for the velocity components parallel ( $V_y$ ) and perpendicular ( $V_x$ ) to the shock front. The profiles are derived by standard SPH summation, e.g. from Eq. (3) for  $\rho$ , and for  $z = 0$ . The vertical distribution of the dense post-shock gas everywhere peaks within 10 pc from that plane.

cerns gas on a larger scale than the 180-pc molecular ring, for which an apparent tilt angle of  $\sim 6^\circ$  has been estimated, also with negative latitude in the first Galactic quadrant (Uchida et al. 1994a; Morris & Serabyn 1996).

Larger tilts of the inner  $\sim 2$  kpc gaseous disc, of  $20^\circ - 30^\circ$  and based on expanding or elliptical motion models, have been reported in the past (e.g. Cohen 1975; Burton & Liszt 1978; Liszt & Burton 1980). More recently, Burton & Liszt (1992) have updated and improved their tilted disc model into a flaring warp with a central disc coplanar to the Galactic plane. The warp is rectilinear in each radius and the tilt of its midplane is given by  $\theta_{\text{max}} \cdot \sin(\phi - \phi_o)$ , where  $\phi$  is the galactocentric azimuth relative to the Sun defined positive in the direction of Galactic rotation,  $\phi_o = 45^\circ$  the azimuth of the line of nodes

and  $\theta_{\max} = 13^\circ$  the maximum tilt angle. This model predicts a tilt angle of about  $4^\circ$  at  $\phi = \varphi_0 = 25^\circ$ , in agreement with the tilt derived for the Galactic dustlanes.

The departure of the dustlanes from the plane  $b = 0$  does not appear to increase linearly with galactocentric distance, but seems to stabilise or gently decline at larger distance, rendering its description by a constant tilt somewhat oversimplistic.

### 6.5. Central molecular zone

This part of the  $\ell - V$  observations is probably the most complex and the most difficult to understand. Binney et al. (1991) have given a detailed description of the gas flow in a rotating barred potential in terms of the closed  $x_1$  orbits, associating the terminal velocity curves in the observed  $\ell - V$  diagrams with the envelope of non self-intersecting such orbits and the parallelogram structure of the 180-pc molecular ring with the innermost orbit of this kind, called the “cusped  $x_1$ ” orbit, where shocks would transform most of the atomic gas into molecules and force the gas to plunge onto the more viable orbits of the  $x_2$  family.

This model is confronted to several problems. The most frequently reported one (e.g. Kuijken 1996; Morris & Serabyn 1996) is the asymmetry of the observed 180-pc parallelogram, and in particular the substantial  $\sim 140 \text{ km s}^{-1}$  forbidden velocity near  $\ell = -0.8^\circ$ , which cannot be fully accounted for by projection effects of the cusped  $x_1$  orbit. Other problems are: (i) when viewed in the full  $\ell - b - V$  data cube, the 180-pc parallelogram appears more as an assemblage of larger scale features rather than forming a distinct unity (see e.g. Fig. 4 in Morris & Serabyn 1996); for instance, its upper edge is observed to extend continuously well beyond the longitude range of the postulated parallelogram and joins the connecting arm through the positive terminal velocity peak, (ii) the terminal velocity peaks and the parallelogram cannot both be generated by the same cusped  $x_1$  orbit because the formers occur well outside the longitude boundaries of the latter, (iii) the longitudinal edges of the parallelogram near  $\ell = -1^\circ$  and  $1.5^\circ$ , assimilated to the bar leading shocks in the model, should define rather clear  $\ell - V$  features as in our models, yet these edges are more disordered than the other edges of the parallelogram, and (iv) the cusped  $x_1$  orbit of the stellar dynamical models in paper I generally does not match the HI terminal velocity peaks; the models providing the best agreement always arise in young and not completely stabilised bars, whereas in older bars the cusped  $x_1$  orbit presents velocity peaks at fairly larger absolute longitudes than observed.

Figure 21 shows that the dustlane shocks are indeed responsible for the positive and negative terminal velocity peaks, but that they do not coincide with the leading edges of the cusped  $x_1$  orbit, which produces velocity peaks at higher absolute longitude and with lower velocity amplitude. Gas on the shocks move along non-periodic orbits with much smaller pericentre than the cusped  $x_1$  orbit. Thus the Milky Way’s cusped  $x_1$  orbit is probably much larger than in the Binney et al. model, explaining why these authors find a very small corotation radius

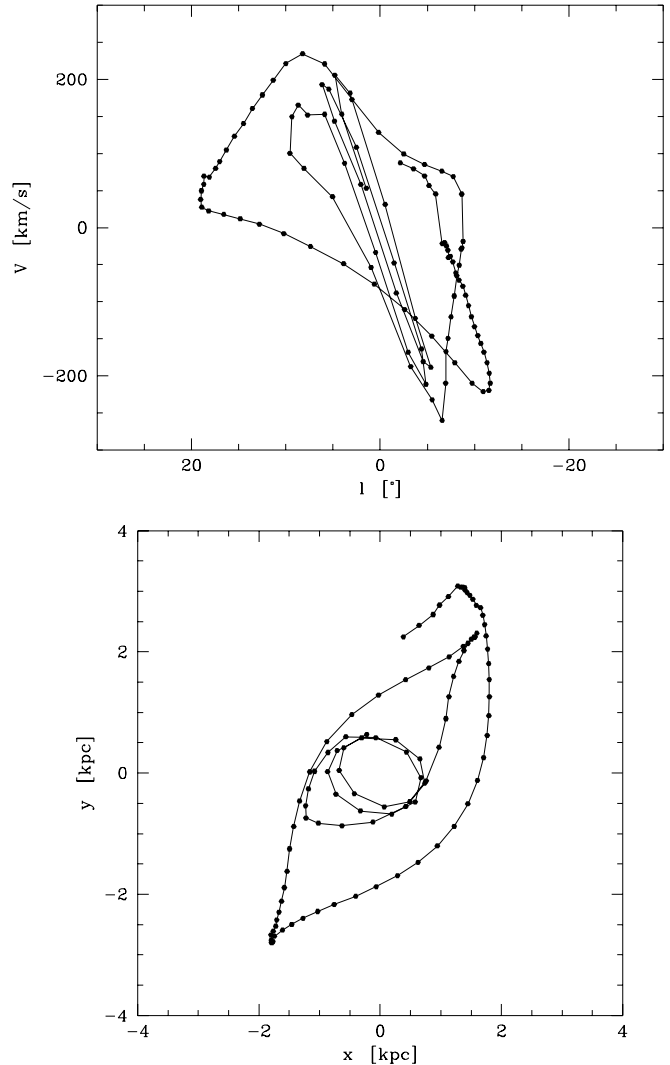


**Fig. 20.** Typical path in the  $x - y$  and  $\ell - V$  planes of an SPH particle in simulation 110. The points show the positions of the particle from  $t = 1994$  to  $2200$  Myr with a constant time interval of 2 Myr. The  $x - y$  plot is in the bar rotating frame with the origin at the density centre and with the bar inclined by  $25^\circ$  relative to  $x = 0$  (like in Fig. 15), and the  $\ell - V$  plot is viewed from  $(x, y) = (0, -8)$  kpc. The particle is chosen to pass through the intersection of the near-side lateral arm and axis shock at  $t = 2066$  Myr, i.e. through  $(x, y) = (-1.4, -2.4)$  kpc in the lower left frame of Fig. 15. Note the larger velocity gap between the points when the particle crosses the far-side axis shock.

of 2.4 kpc. The asymmetries in our models make the cusped  $x_1$  orbit slightly uncertain. In particular, there is a small range of Hamiltonians where the  $x_1$  orbits only loop at one extremity. However, studies of Galactic  $x_1$  orbits generally represent the true Milky Way’s potential by bisymmetric models and therefore are also concerned with similar uncertainties.

The gas on the dustlanes falling onto the nuclear ring from large distances does not necessarily merge with the ring, but

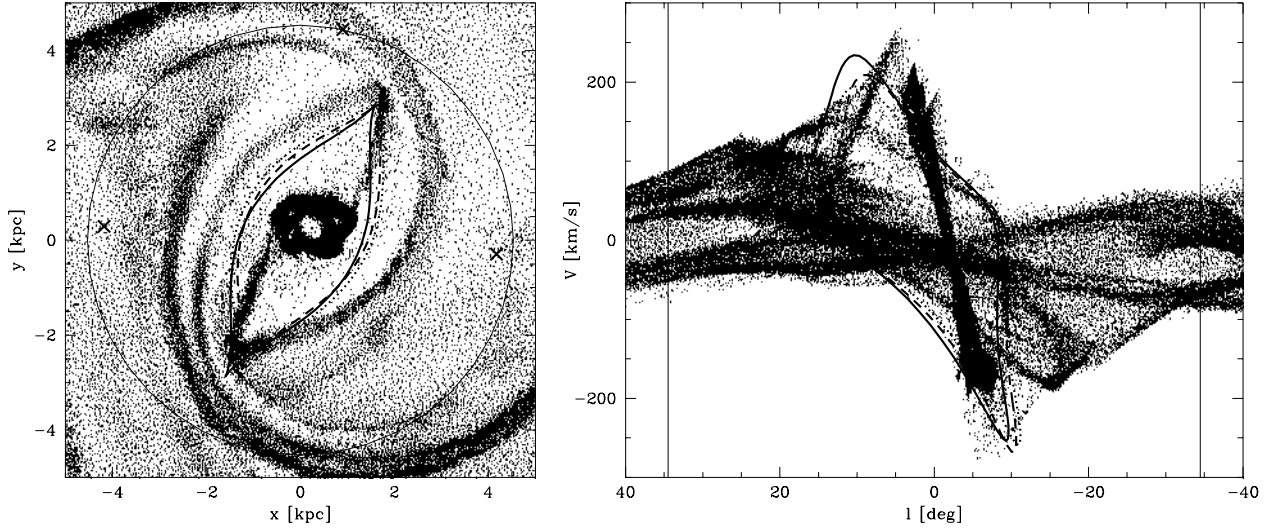


**Fig. 21.** Cusped  $x_1$  orbits in the instantaneous frozen rotating potential, superposed on the spatial gas distribution of model 110t2066 (left), and the corresponding traces in the  $l - V$  diagram (right). The solid line orbit is obtained imposing reflection symmetry on the potential with respect to the vertical axis through the centre of mass, and the other orbits are based on the exact potential rotating about the centre of mass, the dashed and dotted orbits having single cusps at opposite ends. The crosses indicate the Lagrangian points  $L_1$ ,  $L_2$ ,  $L_4$  and  $L_5$ , and the thin solid lines the corotation circle, based on the radius of the Lagrangian points  $L_1$  and  $L_2$ , and the longitudes of its tangent points. Note that in the particle representation used here, the  $l - V$  plot looks different from the one in Fig. 15 because the weights of the inverse squared distance relative to the observer are not taken into account. For example, the molecular ring is more difficult to distinguish without this correction.

rather passes round of it and lands on the opposite dustlane closer to the nuclear ring, merging with it only at the next passage or after repeating the whole cycle once more (Fig. 20; see also Fig. 10a in Fukuda et al. 1998). The farther out the gas on the dustlanes originates, the more it passes away from the nuclear ring. The upper and lower edges of the 180-pc parallelogram could represent such gas streams which precisely brush the nuclear ring/disc, loosing only little mass to it. The mass transfer would appear in the  $l - V$  plot like vertical bridges between the streams and the nuclear disc. An example of such bridges is detectable in the high resolution  $^{12}\text{CO}$  data (e.g. Morris & Serabyn 1996) near  $l = 1.3^\circ$  and for  $V$  between 100 and 200  $\text{km s}^{-1}$ . The brushing streams finally crash in the dustlanes where they are abruptly decelerated. The right longitudinal edge of the 180-pc parallelogram, at  $l \approx -0.8^\circ$ , could be a trace of this process. However it is not very clear why this edge is located at lower absolute longitude than the bright emission near the negative terminal velocity peak, corresponding to gas with about maximum velocity on the far-side dustlane, i.e. why the gas on this dustlane slows down *before* being struck by the positive velocity stream round the nuclear ring. Uchida et al. (1994b) have reported on a large scale shock front in the AFGL 5376 region, which is close to the southern end of the parallelogram upper edge, but which they consider as a support of the expanding molecular ring hypothesis.

## 7. Geometrical constraints on the bar parameters

Figure 22 shows how the  $l - V$  diagram of model 110't2540 changes when the viewing point of the observer is modified. Reducing the bar inclination angle  $\varphi_o$  shrinks the structures longitudinally and amplifies the velocities. The observed knee of the 135- $\text{km s}^{-1}$  arm near  $l = -5^\circ$  is better reproduced, but the transition of the 3-kpc arm to the connecting arm happens at too negative velocity and the connecting arm becomes too steep. Increasing the angle  $\varphi_o$  lowers the forbidden velocities, moves the terminal velocity peaks further away from  $l = 0$  and shifts the connecting arm closer to the northern tangent points of the two molecular ring branches. Increasing the distance of the observer obviously produces a longitudinal contraction, but without modifying the velocity of the structures near the centre. The diagram with the observer at  $\tilde{R}_o = 8$  moves the loop associated to the  $l < 0$  prolongation of the molecular ring structure out to the real tangent point of the Carina arm near  $l = -78^\circ$ . These properties cannot be used to infer a robust inclination angle of the bar because they are based on one specific model and the gas flow is strongly time-dependent.

Constraining the bar parameters by adjusting gas dynamical models to the observed CO and HI  $l - V$  diagrams is a very delicate task and may lead to unreliable results if the models are not sufficiently realistic. However, with our interpretation of the dominant features in these diagrams, it is possible to provide geometrical constraints on the bar inclination angle and extension which do not depend on the details of the models. The principle of the method, illustrated in Fig. 23, is to deter-

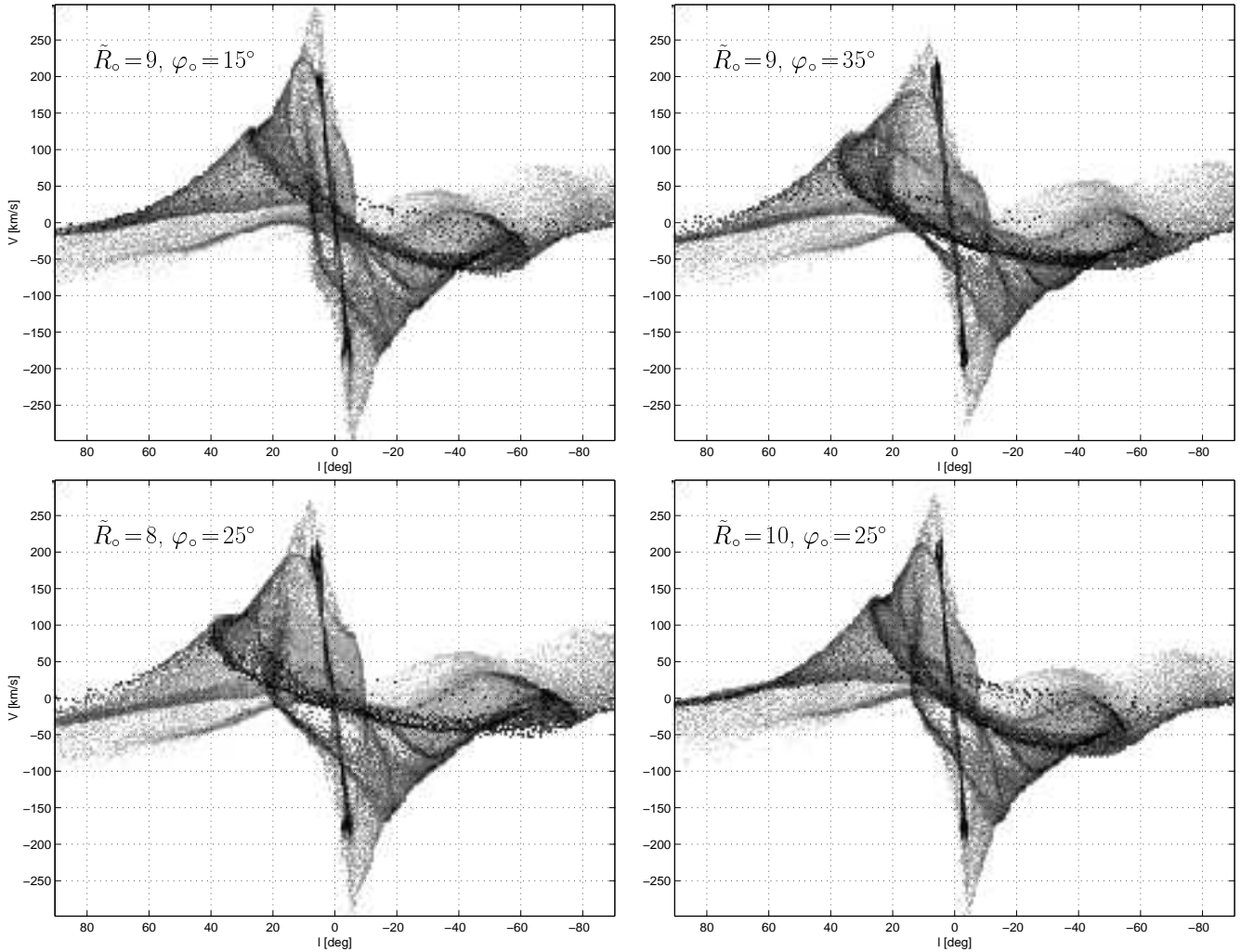


**Fig. 22.** Dependence of the  $l - V$  diagrams on the location of the observer relative to the bar in model 110't2540. The upper diagrams illustrate the effects of changing the bar inclination angle and the lower ones the effects of distance.  $\tilde{R}_o$  represents the galactocentric distance of the observer in initial units, which is 9 in the adopted optimum model displayed in Fig. 15.

mine in the CO and HI data the longitudes  $\ell_1$  and  $\ell_2$  where the 3-kpc and the  $135\text{-km s}^{-1}$  arms intersect the axis shocks and to adjust in real space a major axis through the Galactic centre crossing the line of sights associated to these two directions at galactocentric distances in the ratio  $q \equiv s_1/s_2$ . Simple trigonometrical considerations in the first and fourth Galactic quadrants respectively yield:

$$\frac{s_i}{R_o} = \frac{\sin |\ell_i|}{\sin(\varphi_o + \ell_i)}, \quad i = 1, 2, \quad (26-27)$$

and isolating  $\varphi_o$  and  $s_1$  between these two equations:

$$\tan \varphi_o = -\frac{1+q}{\cot \ell_2 + q \cot \ell_1}, \quad (28)$$

$$\frac{s_1}{R_o} = \left[ (1+q) \frac{\sin^2 \ell_1 + q \sin^2 \ell_2}{\sin^2(\ell_1 - \ell_2)} - q \right]^{1/2}, \quad (29)$$

where  $q$  remains as a parametrisation of the asymmetry level between the lateral arms, which is not a priori known. In the

ideal bisymmetric case  $q = 1$ , but in reality  $q > 1$  according to Sect. 6.2. These formulae rest on the implicit assumption that the intersections of the lateral arms with the axis shocks and the Galactic centre are collinear. If this is wrong, then  $\varphi_o$  will represent the angle between the line joining these intersections and the direction  $\ell = 0$ .

Extrapolating the connecting arm down to the 3-kpc arm in the  $l - V$  observations leads to  $\ell_1 \approx 14.5^\circ$ , where a knee of the 3-kpc arm can be barely detected, whereas the  $135\text{-km s}^{-1}$  arm meets the opposite axis shock at  $\ell_2 \approx -4.5^\circ$  (Fig. 1). The resulting constraints are put together in Fig. 24. Clearly, the distance  $s_1$  increases for smaller values of  $\varphi_o$ , but no precise value can be given so far for the inclination angle. However, the CO data in Fig. 1 betray a second fainter far-side lateral arm which extends down to longitude  $\ell_2 = -7^\circ \pm 0.5^\circ$  with lower forbidden velocities than the  $135\text{-km s}^{-1}$  arm, as well as a quasi-vertical feature at about the same longitude probably corresponding to gas from the same arm plunging towards the nuclear ring/disc after apocentre, on orbits parallel to the

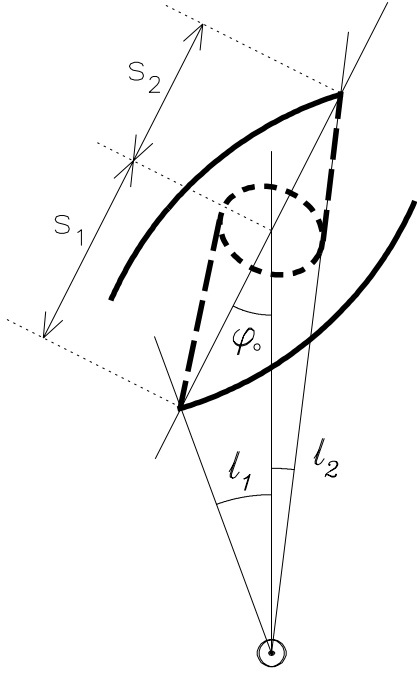


**Fig. 23.** Basic geometry for the localisation of the intersections between the lateral arms (solid lines) and the axis shocks (long dashed lines). The nuclear ring (short dashed line) has been enlarged and the location of the Sun is indicated by the  $\odot$  symbol.

main axis shock. If this is correct, this arm must be much more symmetrical to the 3-kpc arm and the formulae (28) and (29) can be applied to these two arms using  $q = 1$ . The results are  $\varphi_0 = 25^\circ \pm 4^\circ$  and  $s_1 = 3.15$  kpc, and by the way  $q = 1.76$ , i.e.  $s_2 = 1.8$  kpc, for the  $135\text{-km s}^{-1}$  arm.

It remains to see how the arm intersections discussed here are related to the true bar parameters. Numerical simulations and analyses of observations in early-type barred galaxies indicate that the ratio between the bar semi-major axis and the corotation radius amounts to  $a/R_L = 0.85 \pm 0.15$ , and offset dustlanes in such galaxies do not extend beyond the bar ends, i.e.  $s_i \leq a$  (e.g. the review of Elmegreen 1996). Also, bisymmetric hydro simulations in rotating barred potentials with straight offset dustlanes generally have lateral arms intersecting the axis shocks very close to their outer ends and at most a few degrees ahead of the bar major axis. In the standard model 001 of Athanassoula (1992), which has an inner Lindblad resonance but no looped  $x_1$  orbits,  $s/R_L \approx 0.72$ . Adopting  $s_1/R_L = 0.8 \pm 0.1$  as a good compromise, our value of  $s_1$  would imply a corotation radius of  $4.0 \pm 0.5$  kpc for the Milky Way.

The situation in our non-symmetrised and time-dependent simulations, shown in Fig. 25, is much more complicated however. As mentioned in Sect. 5.2, the radius of the intersections between the lateral arms and the axis shocks increases with time. At the formation of a lateral arm, the associated intersection leads the bar major axis, and as the arm moves outwards, it

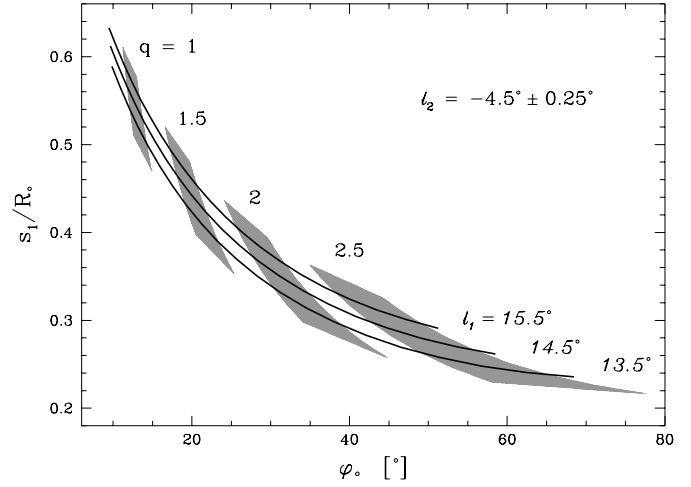


**Fig. 24.** Graphical representation of the geometrical constraints on the bar parameters. The solid curves are derived from Eq. (26) for different values of  $\ell_1$ , and the grey surfaces from Eq. (27) for different values of  $q$ , setting  $s_2 = s_1/q$  and assuming  $-4.75^\circ \leq \ell_2 \leq -4.25^\circ$  to show how uncertainties in  $\ell_2$  propagate to  $q$ .

crosses this axis and becomes trailing. When both are exactly in phase, the intersection radius relative to corotation is 0.75 on the average, compatible with the value adopted above, and compares very well to the apocentre radius of the cusped  $x_1$  orbit (see Fig. 21). Further out, the lateral arms rapidly dissolve in the spiral arms emanating from the very end of the axis shocks. The minimum value of the ratio  $s_i/R_L$ , which could depend on the size of the nuclear ring in the models, is about 0.4. Taking this value as a lower limit for the  $135\text{-km s}^{-1}$  arm leads to  $s_1/R_L = q \cdot s_2/R_L \gtrsim 0.7$  for the 3-kpc arm, suggesting that this arm should meet the connecting arm close to the bar major axis and close to the apocentre of the cusped  $x_1$  orbit. This is also confirmed by the fact that there is no obvious velocity gap in the observed  $\ell - V$  diagrams at the longitude where the 3-kpc arm passes into the connecting arm. Our models suggest that the tangent points of the two molecular ring branches in the first Galactic quadrant are within corotation (see Fig. 21), contrary to Englmaier & Gerhard's (1999) deduction, and therefore we rather advocate  $R_L \geq 4$  kpc.

Our value for the bar inclination angle agrees very well with many other determinations (e.g. Stanek et al. 1997; Nikolaev & Weinberg 1997), and in particular with the recent result  $\varphi_0 = 20^\circ - 25^\circ$  of Englmaier & Gerhard (1999), who derived the gas flow in the potential of the deprojected COBE/DIRBE L-band luminosity distribution (Binney et al. 1997). The bisymmetric hydro simulations done by Weiner & Sellwood (1999) and matched to the observed HI terminal velocity curves favour slightly larger values of this angle, i.e.  $\varphi_0 = 35^\circ \pm 5^\circ$ , and support a corotation radius between 4 and 6 kpc (for  $R_0 = 8.5$  kpc). These authors consider an angle below  $25^\circ$  unlikely, but it should be noted that gas flow fluctuations like those in our self-consistent simulations can increase the  $\ell - V$  area cov-

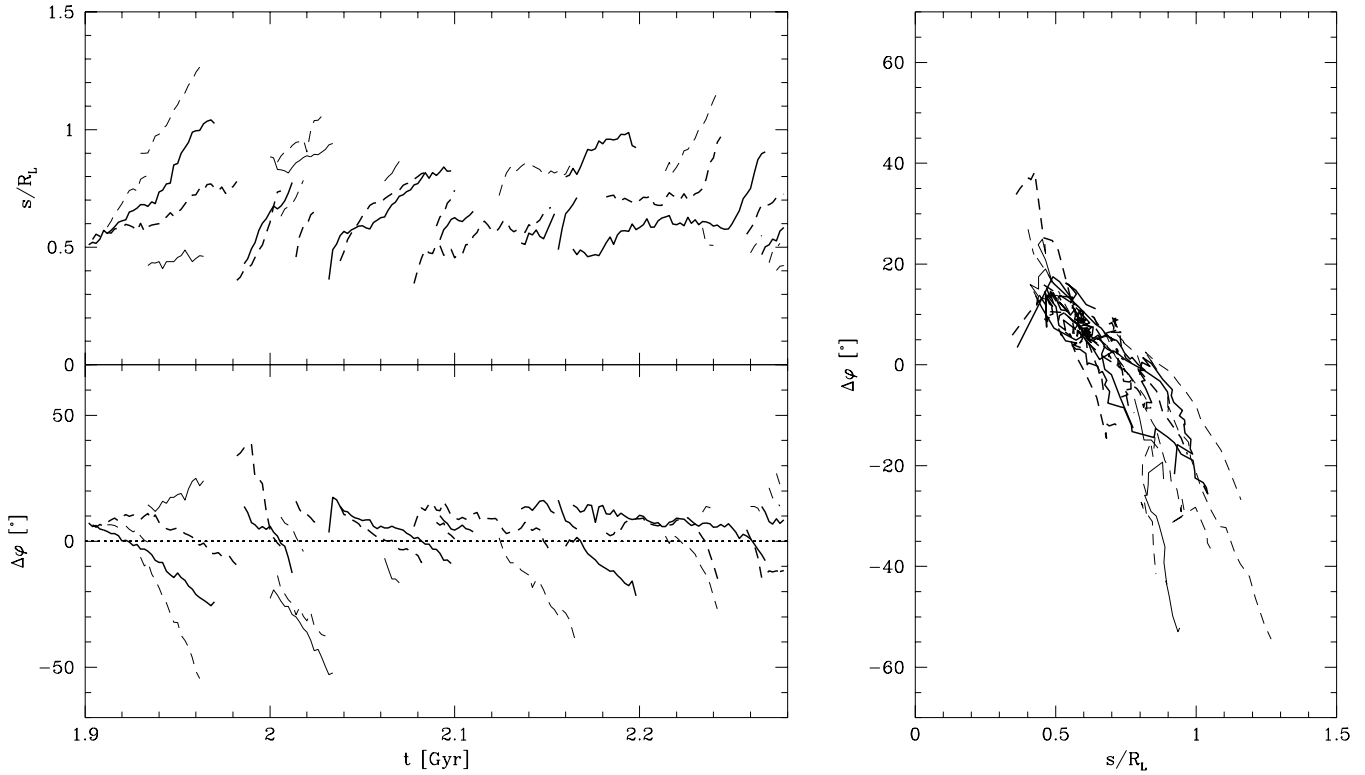


**Fig. 25.** Location of the intersections between the lateral arms and the axis shocks relative to the bar in simulation 110. Left top: distance of these intersections relative to the offcentred density centre and normalised by the corotation radius (based on the Lagrangian points  $L_1$  and  $L_2$ ). Left bottom: phase of the intersections relative to the major axis of the bar, defined positive when the formers lead the latter; the dotted line indicates the locus where both are exactly in phase. Right: correlation between the ordinates of the two previous plots. The solid and dashed lines refer to arm intersections on the same side of the bar, and the bold lines to intersections involving the most contrasted lateral arms.

ered by forbidden velocities and hence substantially bias their method.

It is also possible from our data interpretation to give a crude estimate of the bar pattern speed. If the 3-kpc arm indeed encounters the connecting arm near the apocentre of the cusped  $x_1$  orbit, then the gas at the intersection of the two arms should corotate with the bar figure. Evaluating the radial velocity  $\Delta V$  of this gas relative to the LSR yields its rotation velocity with respect to the Galactic centre:

$$V_c(s_1) = \frac{\Delta V + V_o \sin \ell_1}{\sin(\ell_1 + \varphi_o)}, \quad (30)$$

and resorting to Eq. (26):

$$\Omega_P \equiv \frac{V_c(s_1)}{s_1} = \frac{\Delta V}{R_o \sin \ell_1} + \Omega_o, \quad (31)$$

where  $V_o$  is the circular velocity of the LSR and  $\Omega_o = V_o/R_o$ . The bar inclination angle and  $s_1$  have vanished in this last formula and thus the method is independent of them. The value of  $\Delta V$  is hard to determine in the CO and HI  $\ell - V$  plots because of overlaid emission from the disc and in particular from the molecular ring, but a reasonable range is  $\Delta V = 15 - 35 \text{ km s}^{-1}$ . With  $R_o = 8 \text{ kpc}$ ,  $V_o = 220 \text{ km s}^{-1}$  and  $\ell_1 = 14.5^\circ$  as before, one gets  $\Omega_P = 35 - 45 \text{ km s}^{-1} \text{ kpc}^{-1}$ , in

fair agreement with the  $50 \text{ km s}^{-1} \text{ kpc}^{-1}$  of our gas simulations (Fig. 10) when rescaled to  $R_L = 4.25 \text{ kpc}$ . Changing the value of  $\ell_1$  or  $V_o$  by  $1^\circ$  and  $10 \text{ km s}^{-1}$  modifies the result only by  $\sim 2\%$  and  $3\%$  respectively. However,  $\Delta V$  may be affected by a radial motion of the LSR and/or oscillations of the bar density centre. Longitude-velocity maps of very dense gas (like CS) could help to localise more precisely the transition from the 3-kpc arm to the connecting arm. Note that the method does not apply to the very asymmetric model 110't2540, as can be checked from Fig. 22, because the gas at the transition is not at rest in the frame of the bar.

## 8. Conclusion

This paper presents the first fully self-consistent gas flow models of the inner Milky Way, obtained by incorporating an SPH component with 150 000 particles in realistic symmetry-free barred 3D  $N$ -body simulations with nearly  $4 \times 10^6$  total number of particles. The axisymmetric initial conditions of the simulations are chosen to evolve spontaneously in a barred configuration compatible with the COBE/DIRBE K-band constraints, according to criteria based on a set of lower resolution pure stellar dynamical simulations realised in a precedent paper. The stellar bar rotates with its intrinsic natural pattern speed and the



gas component, gently released from its axisymmetric configuration after the formation of the bar, freely interacts with the live stellar arms.

The density centre of the stellar bar becomes unstable and oscillates around the centre of mass with an amplitude of several 100 pc and a frequency of  $20 - 30 \text{ km s}^{-1} \text{ kpc}^{-1}$ . The gas flow, contrary to other bisymmetric hydro simulations in fixed rotating barred potentials, never reaches a quasi-steady state and can delineate strong asymmetries in its spiral structure, not necessarily induced by the lopsided stellar distribution.

Some models selected from the simulations account for many features seen in the HI and CO longitude-velocity distributions within the Galactic bar and surrounding regions, and provide a very powerful guide to understand the inner structure of the Milky Way. The Galactic bar is inclined by  $25^\circ \pm 4^\circ$  relative to the  $\ell = 0$  line, has a corotation radius of  $4.0 - 4.5 \text{ kpc}$ , a related pattern speed  $\Omega_P \sim 50 \text{ km s}^{-1} \text{ kpc}^{-1}$ , and a face-on axis ratio  $b/a \approx 0.6$ . As in most early-type barred spirals, offset dustlanes are leading the bar major axis. Their gaseous traces in the observed  $\ell - V$  diagrams correspond to the connecting arm (near-side branch) and another feature near  $\ell = -4^\circ$  (far-side branch). These dustlanes are the loci of strong shearing shocks with velocity changes up to  $200 \text{ km s}^{-1}$  across, and are located closer to the bar major axis than the leading edges of the cusped  $x_1$  orbit. The peaks in the terminal velocity curves at  $\ell \approx \pm 2.5^\circ$  are produced by the post-shock gas and not by the  $\ell - V$  trace of the latter orbit, which has velocity peaks at larger absolute longitude and with lower velocity amplitude. The near-side branch of the dustlanes lies below the Galactic plane ( $b < 0$ ) and the other branch, which is seen almost end-on, above it. Their maximum departure from the plane amounts to more than 100 pc.

The 3-kpc and  $135\text{-km s}^{-1}$  arms are the inner prolongations of spiral arms in the disc, each passing close to one bar end and joining by a large bow around the nuclear ring/disc the dustlane in the other side of the bar, at galactocentric distances  $R \approx 3.2 \text{ kpc}$  and  $1.8 \text{ kpc}$  respectively. The  $135\text{-km s}^{-1}$  arm is associated with larger forbidden velocities because of its deeper location in the central potential well.

Velocity-elongated features in the observed CO  $\ell - V$  diagrams “below” the connecting arm, i.e. at similar longitudes but lower velocities than this arm, are interpreted as gas lumps which are just about to cross the shock front layer of the near-side dustlane. A robust example of such a feature is given by the vertical feature near  $\ell = 5.5^\circ$ . Bania’s clump 2 complex is a more controversial candidate because its mean Galactic latitude differs by roughly half a degree from that of the connecting arm at same longitude and because of its substantial mass. Finally, Bania’s clump 1 complex is the part of the  $135\text{-km s}^{-1}$  arm which strikes the far-side dustlane with a considerable incident velocity of order  $100 \text{ km s}^{-1}$ . A fraction of its gas is directly absorbed by the dustlane, producing the apparent positive velocity trace of the dustlane, another fraction is gliding outwards along the dustlane, but the bulk of the clump is probably not intercepted by the dustlane.

The interpretation of the main observed  $\ell - V$  features given in this paper are by far the most plausible that can be deduced from our simulations. However, these simulations may still significantly depart from reality and hence the unicity of our interpretation cannot be guaranteed. For instance, if a large amount of gas is concentrated in the centre, a nuclear fast rotating bar may temporarily form and lead to a different understanding of the very complex innermost gas dynamics.

Some mpeg movies of the gas flow in simulation 110, including live  $\ell - V$  diagrams, are available on the web at <http://obswww.unige.ch/~fux>.

*Acknowledgements.* I would like to thank L. Martinet, D. Pfenniger and D. Friedli for many advices and careful reading of the manuscript, D. Friedli for making its original hybrid  $N$ -body and SPH code available, and F. Combes (referee of this paper), J. Sellwood, O. Gerhard and P. Englmaier for several enlightening discussions. I am also very thankful to T.M. Dame for providing the new high resolution  $\ell - V$   $^{12}\text{CO}$  data, as well as to B.W. Burton, S. West, H. Liszt, S. Digel and J. Ohmacher for their help in reassembling the necessary HI surveys for a full  $\ell - b - V$  coverage of the Galactic plane region. This work was mainly supported by the Swiss National Science Foundation.

## References

- Athanassoula E. 1992, MNRAS 259, 345  
 Bally J., Stark A.A., Wilson R.W., Henkel C. 1987, ApJS 65, 13  
 Bally J., Stark A.A., Wilson R.W., Henkel C. 1988, ApJ 324, 223  
 Balsara D.S. 1995, J. Comput. Phys. 121, 357  
 Bania T.M. 1977, ApJ 216, 381  
 Bania T.M., Stark A.A., Heiligman G.M. 1986, ApJ 307, 350  
 Benz W. 1990. In: Buchler J.R. (ed.) NATO ASI Ser. C 302, The Numerical Modelling of Nonlinear Stellar Pulsations. Kluwer, Dordrecht, p. 269  
 Berentzen I., Heller C.H., Shlosman I., Fricke K.J. 1998, MNRAS 300, 49  
 Binney J., Gerhard O.E., Stark A.A., Bally J., Uchida K.I. 1991, MNRAS 252, 210  
 Binney J., Gerhard O., Spergel D. 1997, MNRAS 288, 365  
 Blitz L. 1993. In: Holt S.S., Verter F. (eds.) AIP Conf. Proc. 278, Back to the Galaxy. AIP, New York, p. 98  
 Blitz L., Spergel D.N. 1991, ApJ 379, 631  
 Block D.L., Bertin G., Stockton A. et al. 1994, A&A 288, 365  
 Burke B.F., Tuve M.A. 1964. Kerr F.J., Rodgers A.W (eds.) IAU-URSI Symp. 20, The Galaxy and the Magellanic Clouds. Australian Academy of Science, Canberra, p. 183  
 Burton W.B. 1973, PASP 85, 679  
 Burton W.B. 1985, A&AS 62, 365  
 Burton W.B. 1992. In: Pfenniger D., Bartholdi P. (eds.) Saas-Fee Advanced Course 21, The Galactic Interstellar Medium. Springer, Berlin  
 Burton W.B., Liszt H.S. 1978, ApJ 225, 815  
 Burton W.B., Liszt H.S. 1992, A&AS 95, 9  
 Buta R. 1996. In: Buta R., Crocker D.A., Elmegreen B.G. (eds.) Proc. IAU Coll. 157, ASP Conf. Ser. 91, Barred Galaxies. ASP, San Francisco, p. 11  
 Cohen R.J. 1975, MNRAS 171, 659  
 Cohen R.J., Davies R.D. 1976, MNRAS 175, 1  
 Cohen R.J., Few R.W. 1976, MNRAS 176, 495  
 Colin J., Athanassoula E. 1989, A&A 214, 99

- Combes F. 1991, *ARA&A* 29, 195
- Contopoulos G., Mertzaniades C. 1977, *A&A* 61, 477
- Cowie L.L. 1980, *ApJ* 236, 868
- Dame T.M., Ungerechts H., Cohen R.S. et al. 1987, *ApJ* 322, 706
- Dame T.M., Hartmann D., Thaddeus P. 1999, *ApJ* (in preparation)
- Dwek E., Arendt R.G., Hauser M.G. et al. 1995, *ApJ* 445, 716
- Elmegreen B. 1996. In: Buta R., Crocker D.A., Elmegreen B.G. (eds.) *Proc. IAU Coll. 157, ASP Conf. Ser. 91, Barred Galaxies*. ASP, San Francisco, p. 197
- Englmaier P., Gerhard O. 1997, *MNRAS* 287, 57
- Englmaier P., Gerhard O. 1999, *MNRAS* (in press)
- Evans N.W. 1994, *ApJ* 437, L31
- Fehlberg E. 1968, *NASA Technical Report TR-R287*
- Friedli D. 1992, PhD Thesis 2553, Geneva Observatory, Geneva
- Friedli D., Benz W. 1993, *A&A* 268, 65
- Fukuda H., Wada K., Habe A. 1998, *MNRAS* 295, 463
- Fux R. 1997, *A&A* 327, 983 (paper I)
- Gerhard O.E. 1996. In: Blitz L., Teuben P. (eds.) *Proc. IAU Symp. 169, Unsolved Problems of the Milky Way*. Kluwer, Dordrecht, p. 79
- Gerhard O.E., Vietri M. 1986, *MNRAS* 223, 377
- Gyuk G. 1999, *ApJ* 510, 205
- Hartmann D., Burton W.B. 1997, *Atlas of Galactic Neutral Hydrogen*. Cambridge Univ. Press, Cambridge, New York
- Hockney R.W., Eastwood J.W. 1981, *Computer Simulation Using Particles*. McGraw-Hill, U.S.A.
- Humphreys R.M., Larsen J.A. 1995, *AJ* 110, 2183
- Hut P., Makino J., McMillan S. 1995, *ApJ* 443, L93
- Izumiura H., Deguchi S., Hashimoto O. et al. 1994, *ApJ* 437, 419
- Jackson J.M., Heyer M.H., Paglione T.A.D., Bolatto A.D. 1996 *ApJ* 456, L91
- Joersaeter S., van Moorsel G.A. 1995, *AJ* 110, 2037
- Kaifu N., Kato T., Iguchi T. 1972, *Nature Phys. Sci.* 238, 105
- Kerr F.J. 1967. In: van Woerden H. (ed.) *Proc. IAU Symp. 31, Radio Astronomy and the Galactic System*. Academic Press, London, p. 239
- Kerr F.J., Bowers P.F., Kerr M., Jackson P.D. 1986, *A&AS* 66, 373
- Kuijken K. 1996. In: Buta R., Crocker D.A., Elmegreen B.G. (eds.) *Proc. IAU Coll. 157, ASP Conf. Ser. 91, Barred Galaxies*. ASP, San Francisco, p. 504
- Laine S., Kenney J.D.P., Yun M.S., Gottesman S.T. 1999, *ApJ* (in press)
- Lee C.W. 1996, *ApJS* 105, 129
- Levine S.E., Sparke L.S. 1998, *ApJ* 496, L13
- Lindblad P.O., Hjelm M., Hoegbom J. et al. 1996, *A&AS* 120, 403
- Liszt H.S., Burton W.B. 1978, *ApJ* 226, 790
- Liszt H.S., Burton W.B. 1980, *ApJ* 236, 779
- Merrifield M.R. 1992, *AJ* 103, 1552
- Miller R.H., Smith B.F. 1992, *ApJ* 393, 508
- Monaghan J.J. 1992, *ARA&A* 30, 543
- Morris M., Serabyn E., 1996, *ARA&A* 34, 645
- Mulder W.A., Liem B.T. 1986, *A&A* 157, 148
- Nakada Y., Deguchi S., Hashimoto O. et al. 1991, *Nature* 353, 140
- Nikolaev S., Weinberg M.D. 1997, *ApJ* 487, 885
- Oka T., Hasegawa T., Hayashi M., Handa T., Sakamoto S. 1998a, *ApJ* 493, 730
- Oka T., Hasegawa T., Sato F., Tsuboi M., Miyazaki A. 1998b, *ApJS* 118, 455
- Oort J.H. 1977, *ARA&A* 15, 295
- Paczynski B., Stanek K.Z., Udalski A. et al. 1994, *ApJ* 435, L113
- Pence W.D., Blackman C.P. 1984, *MNRAS* 207, 9
- Peters W.L. 1975, *ApJ* 195, 617
- Pfenniger D., Friedli D. 1993, *A&A* 270, 561
- Raboud D., Grenon M., Martinet L., Fux R., Udry S. 1998, *A&A* 335, L61
- Regan M.W., Vogel S.N., Teuben P.J. 1997, *ApJ* 482, L143
- Reynaud D., Downes D. 1998, *A&A* 337, 671
- Roberts W.W., Huntley J.M., van Albada G.D. 1979, *ApJ* 233, 67
- Rougoor G.W. 1964, *BAN* 17, 381
- Rougoor G.W., Oort J.H. 1960, *Proc. Nat. Acad. Sci.* 46, 1
- Rudnick G., Rix H.W. 1998, *AJ* 116, 1163
- Sackett P.D. 1997, *ApJ* 483, 103
- Sandage A., Bedke J. 1988. *NASA SP-496, Atlas of Galaxies*. NASA, Washington
- Schoenmakers R. 1999. In: Merritt D.R., Valluri M., Sellwood J.A. (eds) *ASP Conf. Ser., Galaxy Dynamics* (in press)
- Scoville N.Z. 1972, *ApJ* 175, L127
- Scoville N.Z. 1992. In: Maran S.P. (ed.) *The A&A Encyclopedia*. Cambridge Univ. Press, Cambridge, p. 373
- Sellwood J.A., Sparke L.S. 1988, *MNRAS* 231, L25
- Sevenster M.N. 1996. In: Buta R., Crocker D.A., Elmegreen B.G. (eds.) *Proc. IAU Coll. 157, ASP Conf. Ser. 91, Barred Galaxies*. ASP, San Francisco, p. 536
- Shane W.W. 1972, *A&A* 16, 118
- Simonson S.C., Mader G.L. 1973, *A&A* 27, 337
- Sofue Y. 1995, *PASJ* 47, 527
- Stanek K.Z., Udalski A., Szymanski M. et al. 1997, *ApJ* 477, 163
- Stark A.A., Bania T.M. 1986, *ApJ* 306, L17
- Stark A.A., Gammie C.F., Wilson R.W. et al. 1992, *ApJS* 79, 77
- Steinmetz M. 1996, *MNRAS* 278, 1005
- Uchida K.I., Morris M., Bally J. 1994a. In: Genzel R., Harris A.I. (eds.) *NATO ASI Ser. C 445, The Nuclei of Normal Galaxies: Lessons from the Galactic Center*. Kluwer, Dordrecht, p. 99
- Uchida K.I., Morris M.R., Serabyn E., Bally J. 1994b, *ApJ* 421, 505
- Vallée J.P. 1995, *ApJ* 454, 119
- van Albada G.D. 1985. In: van Woerden H., Allen R.J., Burton W.B. (eds.) *Proc. IAU Symp. 106, The Milky Way Galaxy*. Reidel, Dordrecht, p. 547
- van der Kruit P.C. 1970, *A&A* 4, 462
- van der Kruit P.C. 1971, *A&A* 13, 405
- van der Kruit P.C. 1988, *A&A* 192, 117
- van der Kruit P.C., Shostak G.S. 1984, *A&A* 134, 258
- van der Kruit P.C., Oort J.H., Mathewson D.S. 1972, *A&A* 21, 169
- van Woerden H., Rougoor G.W., Oort J.H. 1957, *Comptes Rendus Acad. Sci. Paris* 244, 1961.
- Wada K., Taniguchi Y., Habe A., Hasegawa T. 1994, *ApJ* 437, L123
- Weiland J.L., Arendt R.G., Berriman G.B. et al. 1994, *ApJ* 425, L81
- Weinberg M.D. 1992, *ApJ* 384, 81
- Weinberg M.D. 1994, *ApJ* 421, 481
- Weiner B.J., Sellwood J.A. 1999, submitted to *ApJ*
- Weiner B.J., Williams T.B., Sellwood J.A. 1993, *BAAS* 183, 76.07
- Whitlock P., Catchpole R. 1992. In: Blitz L. (ed.) *Astroph. and Space Sci. Library* 180, *The Center, Bulge and Disk of the Milky Way*. Kluwer, Dordrecht, p. 103
- Zhao H.S., Mao S. 1996, *MNRAS* 283, 1197
- Zhao H.S., Rich R.M., Spegel D.N. 1996, *MNRAS* 282, 175